Sound emission in a quasi-steady transonic turbulent flow past a circular cylinder

Sound emission in a quasi-steady transonic turbulent flow past a circular cylinder

Shuai Li [*]
Division of Fluid Dynamics, Department of Mechanics and Maritime Sciences, Chalmers University of Technology, SE-412 96 Gothenburg, Sweden

(Received 2 June 2024; accepted 7 February 2025; published 10 March 2025)

This study investigates the noise generation mechanism of a circular cylinder in a quasi-steady transonic condition using direct noise computation. Unlike a subsonic circular cylinder, where noise is generated by alternate vortex shedding, it is found that in a quasi-steady condition, where vortex shedding is suppressed, the cylinder noise is primarily generated by the oscillation of separated shear layers, also known as shear layer instability. The flow contains complex features such as weak oblique shocks, expansion fans, fluctuating separated shear layers, suppressed vortex shedding, λ shocks, and quasi-steady bow shocks. Near-wake pressure fluctuations are found to be more strongly correlated with far-field pressure fluctuations, whereas wall pressure fluctuations are uncorrelated with far-field pressure fluctuations, suggesting that the sound sources are located in the near wake rather than on the cylinder surface. In the downstream far field, a dominant tone at the frequency of the fluctuating separated shear layers is observed. In the near-field region just behind the λ shocks, as the distance from the fluctuating separated shear layer increases, the acoustic pressure fluctuation replaces the hydrodynamic pressure fluctuation as the dominant component. In the region of expansion fans, the pressure fluctuation is mainly low-frequency acoustic pressure fluctuation. In the region of fluctuating separated shear layers, while the pressure fluctuation includes similar amounts of acoustic and hydrodynamic components at most frequencies, it predominantly consists of acoustic component at the frequency of the fluctuating separated shear layers. Overall, the dominant acoustic waves are primarily generated by the oscillation of the separated shear layers. Among the various-scale vortical structures, the one induced by the oscillation of the separated shear layers is most closely associated with both sound and pseudo-sound signatures.

DOI: 10.1103/PhysRevFluids.10.034603

I. INTRODUCTION

The flow around a circular cylinder is fundamentally interesting due to its canonical representation of many bluff-body flows, such as flows past aircraft fuselages, engine nacelles and landing gears. Numerous studies have investigated incompressible or low-Mach-number cylinder flows, focusing on aspects such as wakes [1–4], transition to turbulence [5–8], vortex shedding [9], aerodynamic forces [10], and sound generation [11–14]. For comprehensive reviews, readers may refer to Berger and Wille [15], Norberg [16], and Williamson [17]. Under incompressible and

[*]Contact author: shuai.li@chalmers.se

low-Mach-number conditions, vortex shedding occurs as a result of shear layer instability. As this instability develops, the shear layer rolls up to form a vortex, which continues to grow as it is fed by circulation from the shear layer. This feeding process continues until the vortex becomes strong enough to draw the opposite shear layer across the wake. Once the vortex is no longer supplied with circulation, it detaches and is shed into the downstream wake [18,19]. As the flow enters the transonic regime, many flow features, such as the separated flow, become even more complex. Mani *et al.* [20] and Mani [21] performed large eddy simulations (LESs) of transonic flow past a circular cylinder at $\mathrm{Re} = 10^4$ and $\mathrm{Ma} = 0.85$. Here it was observed that the flow accelerates over the front portion of the circular cylinder, experiencing a weak shock which intersects with the cylinder surface at the separation point. The weak shock acts to redirect the separated flow while the unsteady accelerated flow still remains supersonic. Further downstream, the supersonic flow returns to the subsonic regime across a normal shock. Recently, Couliou and Brion [22] performed a wind-tunnel experiment across a range of Mach numbers $0.3 \leqslant \mathrm{Ma} \leqslant 0.85$ and corresponding Reynolds numbers $2 \times 10^5 \leqslant \mathrm{Re} \leqslant 5 \times 10^5$ to investigate the transition of wake states in transonic flows past a circular cylinder. They observed three different wake states, namely, the vortex shedding state, the parallel shear layer state, and the crossed shear layer state, in a narrow range of Mach numbers between 0.8 and 0.85. They also found that the transitions between these wake states have a hysteresis behavior.

It is commonly known that, starting at $\mathrm{Ma} = 0.9$, the flow transitions to a quasi-steady state such that vortex shedding ceases. Murthy and Rose [23,24] investigated vortex-shedding frequencies, form drag, and skin friction through a series of wind-tunnel tests at Mach numbers $0.25 \leqslant \mathrm{Ma} \leqslant 1.2$ and Reynolds numbers $\mathrm{Re} = 3 \times 10^4$, 1.66×10^5, and 5×10^5. They observed that detectable periodic vortex shedding ceases above $\mathrm{Ma} = 0.9$. Xu *et al.* [25,26] performed detached eddy simulations (DESs) of transonic flows over a circular cylinder at a Reynolds number of $\mathrm{Re} = 2 \times 10^5$ and at Mach numbers of $\mathrm{Ma} = 0.85$, 0.88, 0.9, and 0.95. The flow states were found to be unsteady for $\mathrm{Ma} < 0.9$ and quasi-steady for $\mathrm{Ma} > 0.9$, respectively. The unsteady flow state is characterized by complex interactions between moving shock waves and turbulent flow in the near field of the circular cylinder, whereas the quasi-steady flow state is characterized by suppressed vortex shedding and nearly stationary shock waves. Xia *et al.* [27] conducted constrained large eddy simulations (CLESs) of a circular cylinder at a subcritical Reynolds number of $\mathrm{Re} = 4 \times 10^4$ and a supercritical Reynolds number of $\mathrm{Re} = 1 \times 10^6$, with Mach numbers ranging from $0.5 \leqslant \mathrm{Ma} \leqslant 0.95$. For $\mathrm{Ma} \geqslant 0.9$, no apparent vortex shedding was detected, and the flow state becomes quasi-steady. It was also observed that the separated shear layers tended to converge in the wake for $\mathrm{Ma} \geqslant 0.9$.

The sound emitted from a circular cylinder is closely related to the near-field flow features. In subsonic conditions, it is well known that sound-pressure waves are generated primarily by alternate vortex shedding [11]. In the near field, the pressure fluctuations generated on the cylinder surfaces and those generated in the oscillating flow just behind a cylinder due to vortex shedding are sound sources [11,13,28]. In the far field, the propagating sound waves show a dipole pattern, which consists of a fundamental tone and several harmonics [11,12,14,29–32]. In transonic conditions, studies on sound emitted from a circular cylinder remain scarce. Rodriguez [33] conducted wind-tunnel experiments at transonic Mach numbers of 0.75 and 0.85, and at a Reynolds number of approximately 10^5 at which the boundary-layer separation process is still laminar. It was shown that unsteady pressure mainly consists of a fundamental tone and its first harmonic. Around the greater part of the circular cylinder, the former strongly dominates over the latter. Close to the plane of symmetry, the former decreases dramatically and the latter becomes dominant. Tamura and Tsutahara [28] performed direct numerical simulations (DNSs) to investigate the sound generation and radiation in laminar flows at $\mathrm{Re} = 150$ and 200 with Mach numbers ranging from $0.2 \leqslant \mathrm{Ma} \leqslant 0.9$. At $\mathrm{Ma} = 0.9$, they observed that the sound is generated by the interaction between the shock waves and the wake vortices, and that the sound radiates only in the downstream direction. Although the issue of overall sound generation in transonic conditions was considered by Rodriguez [33] and by Tamura and Tsutahara [28], there has been no study relating

sound sources with the various transonic cylinder near-field flow features, i.e., formation of weak oblique shocks, expansion fans, compression waves, fluctuating separated shear layers, suppressed vortex shedding, λ shocks, and quasi-steady bow shocks. More importantly, the literature has been silent on the issue of quantitatively separating the radiating acoustic pressure fluctuations from the nonradiating hydrodynamic pressure fluctuations for a transonic cylinder flow. The objective of this paper is therefore to study how sound is generated when detectable vortex shedding ceases at $\mathrm{Ma} = 0.9$, and to quantitatively assess the radiating sound and nonradiating pseudo-sound generated by the aforementioned flow features, as well as the sound and pseudo-sound signatures associated with various scales of turbulent structures. The separation between radiating acoustic pressure fluctuations and nonradiating hydrodynamic pressure fluctuations is accomplished through the wavelet decomposition of near-field pressure fluctuations, which has previously been applied in subsonic jets and cylinder flows [31,34–37].

In the present study, a three-dimensional DNS of transonic flow past a circular cylinder at $\mathrm{Re} = 3900$ and $\mathrm{Ma} = 0.9$ is performed. Section II is devoted to a description of the numerical methods, simulation setup, the wavelet decomposition technique of Mancinelli *et al.* [37], and wavelet multiresolution analysis. Key findings of this study are presented in Sec. III. More specifically, results pertaining to the cylinder near-field flow dynamics, far-field sound propagation, and the correlation of far-field pressure fluctuations with both cylinder wall and near-wake pressure fluctuations are discussed in Secs. III A–III C, respectively. The wavelet decomposition of pressure fluctuations in the region just behind the λ shocks, as well as those in the region of the expansion fan, in the region of the fluctuating separated shear layers, and in the far field near the wake, are presented in Secs. III D–III F, respectively. Section III G is devoted to the analysis of the sound and pseudo-sound signatures associated with various scales of turbulent structures. Finally, conclusions are summarized in Sec. IV.

II. METHODOLOGY

A. Numerical methods

The three-dimensional unsteady compressible Navier-Stokes equations in curvilinear form are solved using a high-order finite-difference method. The numerical algorithm consists of sixth-order compact schemes of Lele [38] in combination with third- and fourth-order boundary schemes for the spatial discretization as well as the interpolation between staggered and collocated grid nodes. For time advancement, a second-order fully implicit method of Beam and Warming [39] is used for the near-wall region, while a third-order explicit three-step Runge-Kutta scheme is used for the region far from the wall. Adiabatic, no-slip, and no-penetration boundary conditions are applied at the wall. Periodic boundary conditions are adopted in the spanwise direction. For the present simulation of a spatially developing flow, the inflow boundary conditions of Giles [40] and outflow boundary conditions of Collis [41] are adopted. A shock treatment based on the artificial bulk viscosity is applied in the shock-containing region [20]. In addition, a sponge layer, which consists of a dissipation term added to the governing equations, is applied at the outer boundary to silently damp the outgoing disturbances. See Nagarajan *et al.* [42] for more details of the present in-house code and Mani *et al.* [20,43,44], Khalighi *et al.* [12], and Li *et al.* [31] for applications of this code in simulating subsonic flows past a circular cylinder.

B. Simulation setup

The simulation domain is cylindrical in shape with a diameter of about $91D$ and a spanwise length of πD where D is the diameter of the circular cylinder. The circular cylinder is positioned $9D$ upstream of the computational domain center, making the downstream region longer than the upstream region. This is beneficial because sound generation and propagation primarily occur in the downstream direction in the present investigation. The present grid configuration,as shown in Fig. 1, is a symmetric body-fitted O grid consisting of $640 \times 1151 \times 96$ grid nodes

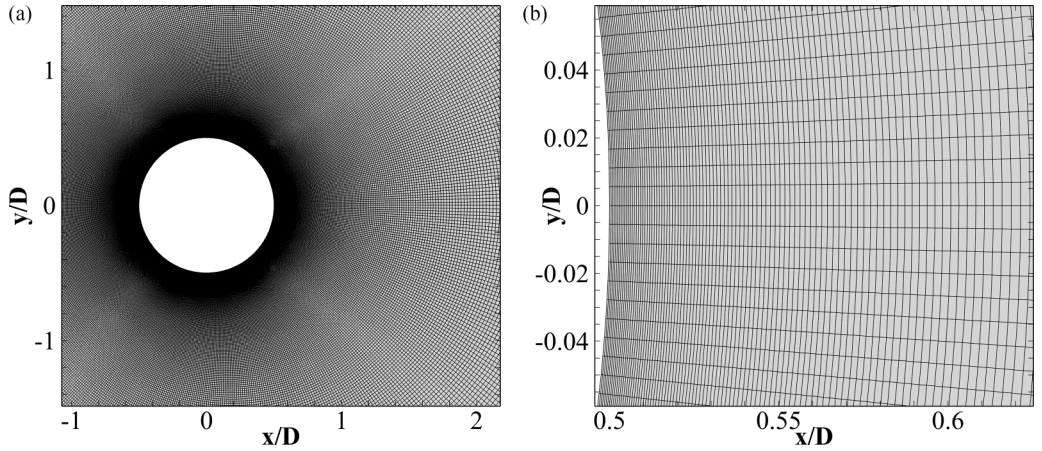

FIG. 1. A symmetric body-fitted O grid for a circular cylinder: (a) the mesh in the near field of the cylinder and (b) a close-up around the rear base point of the cylinder.

in the circumferential, wall-normal, and spanwise directions, respectively. The spacing of the first grid point in the wall-normal direction is $\delta_{1st} = 0.0003D$ at the leading edge of the circular cylinder, which stretches to $\delta_{far} = 0.06D$ at the downstream outflow boundary. The present computational grid has been previously used in the DNS of a circular cylinder at the same Reynolds number (Re = 3900) but at lower Mach numbers (Ma = 0.2 and 0.4) [31]. This mesh is finer than those used in other DNS studies of a circular cylinder at the same or similar Reynolds number [45,46].

A DNS of a uniform flow past a stationary cylinder is performed at Ma = 0.9 and Re = 3900 based on the freestream velocity and diameter of the cylinder. Given that spanwise periodic boundary conditions are used in the present simulation, it is important to note that the acoustic field obtained from numerical simulations with spanwise periodic boundary conditions is quite different from that radiated by a cylinder of a finite span. In fact, the tone level of a finite-span circular cylinder follows a sigmoidal trend: for very short and very long cylinders, the effect of length on sound levels diminishes, approaching an asymptote. For cylinders of intermediate length (between $10D$ and $30D$), the sound level rises sharply with increasing span [47]. Additionally, for cylinders shorter than $20D$, the tone frequency varies with length, closely following a fourth-degree polynomial relationship [48]. In the present simulation, after the initial transient stage of the simulation, the time series of the pressure signal is sampled for 245 000 time steps, with a constant time step of $\Delta t = 2.78 \times 10^{-3} D/c_\infty$. With this sampling rate, the Nyquist criterion is well satisfied. Figure 2 shows the distribution of the sampling positions from the cylinder near field to the far field with the circular cylinder located at the origin. The sampling positions are distributed along different radial lines from the upstream to downstream centerline with an increment of 10° and along different half circles with their centers gradually going downstream in order to coincide with the mesh. Given that the sampling positions are distributed on radial lines at different polar angles, hereinafter, polar coordinate (r, θ), rather than cartesian coordinates, will be used to describe the sampling positions. In the polar coordinate, r and θ are the radial distance from the origin and the angle with the upstream centerline, respectively.

C. Wavelet decomposition technique and multiresolution analysis

The continuous wavelet transform (CWT) of a pressure fluctuation signal $p'(t)$ consists of a projection onto a basis of compact support functions obtained through the dilation and translation of the mother wavelet $\Psi(t)$. The wavelet coefficient w, as a function of the resolution time scale (s)

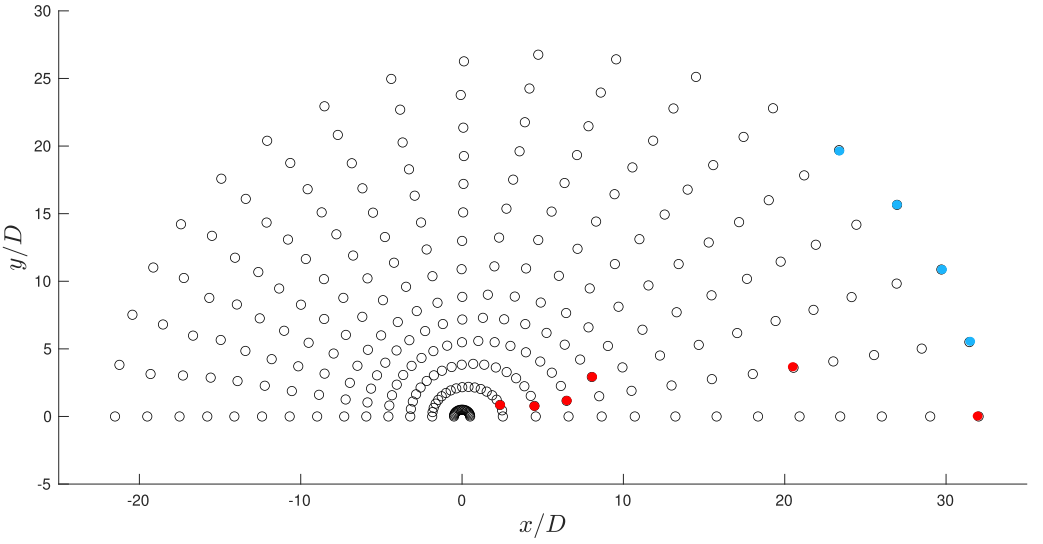

FIG. 2. Sampling positions distributed on 14 half circles from the cylinder surface to its far field. From left to right, the six probes in red are located at (2.5D, 160°), (4.6D, 170°), (6.6D, 170°), (8.6D, 160°), (20.9D, 170°), and (32D, 180°), respectively. Clockwise, the four probes in blue are located at (30.6D, 140°), (31.2D, 150°), (31.6D, 160°), and (31.9D, 170°), respectively.

and the translation time (t), is obtained by [49]

$$w(s,t) = C_\Psi^{-1/2} s^{-1/2} \int_{-\infty}^{\infty} \Psi^*\left(\frac{\tau - t}{s}\right) p'(\tau)\, d\tau, \tag{1}$$

where $\Psi^*((\tau - t)/s)$ is the complex conjugate of the dilated and translated mother wavelet $\Psi(t)$ and $C_\Psi^{-1/2}$ is a constant to take into account the average value of $\Psi(t)$. Similarly, the wavelet coefficient of the discrete wavelet transform (DWT) is obtained as follows [49]:

$$w^{(s)}(n) = \sum_{i=-\infty}^{\infty} g^{(s)}(n - 2^s i) p'(i), \tag{2}$$

where s is the discretized scale and $g^{(s)}(i)$ represents the discrete version of $\Psi^{(s)}(t)$.

The decomposition of near-field pressure fluctuations into acoustic and hydrodynamic components is accomplished by applying a proper threshold to the wavelet coefficients. According to Mancinelli *et al.* [37], their first wavelet decomposition technique requires an additional far-field pressure fluctuation signal to separate the near-field pressure fluctuation. The physical basis of such a decomposition technique is that the hydrodynamic pressure fluctuation decays rapidly as the distance increases, and that the near-field acoustic pressure fluctuation is the only component to reach the far field and thus correlates well with the far-field sound [37,50]. On one hand, the hydrodynamic component attenuates rapidly with distance [50,51] and is largely unaffected by fluid compressibility [52]. This component contains local information concerning localized turbulent structures and is thus heavily influenced by the turbulence in the flow [36]. Consequently, hydrodynamic pressure fluctuations compress well on a wavelet basis. On the other hand, the acoustic component attenuates more slowly with distance. It is associated with sound waves that propagate at the speed of sound and follows the linear wave equation [37,53]. Starting from an initial guess of the threshold,

$$T_0 = \sqrt{2\langle p'^2 \rangle \log_2 N_s}, \tag{3}$$

where $\langle p'^2 \rangle$ and N_s are the variance and length of the pressure fluctuations, respectively. The threshold for the decomposition procedure is updated iteratively until the separated acoustic pressure fluctuation correlates best with the far-field sound. Choosing this initial threshold T_0 provides a minimax solution to the problem of minimizing the ideal mean squared error (MSE) between the estimator and the signal without noise. With this T_0, the thresholding rule yields a mean squared error (or risk) that remains consistently less than a constant multiplied the sum of the squared noise level and the ideal MSE [54,55]. Based on the guessed threshold in each iterative process, the near-field pressure fluctuation is decomposed into acoustic and hydrodynamic components. It is then straightforward to compute the cross-correlation coefficient between the far-field pressure fluctuation and the guessed separated acoustic component of the near-field pressure fluctuation. Once the maximum cross-correlation coefficient peak is found, the threshold corresponding to this peak is selected for the decomposition procedure. During the decomposition procedure, the wavelet coefficients greater than the selected threshold in absolute value correspond to the hydrodynamic component. The acoustic component is thus the remaining part of the pressure fluctuation. Since the separated acoustic pressure fluctuations are radiating, they are also known as sound. The separated hydrodynamic pressure fluctuations are nonradiating. Therefore, they are referred to as pseudo-sound by Ribner [51]. The reader may refer to Mancinelli *et al.* [37] for more details of the wavelet decomposition technique used in the present study.

For the multiresolution analysis, the pressure fluctuation signal $p'(t)$ discretized at N_s points can be decomposed into $L + 1$ components, including a coarse-scale approximation A_L and L detailed components D_i of the signal, as follows [56–59]:

$$p'(t) = A_L + \sum_{i=1}^{L} D_i, \tag{4}$$

where A_L and D_i can be expressed as

$$A_L = \sum_{k=0}^{N_s-1} c_k 2^{-L/2} \Phi(2^{-L}t - k), \tag{5}$$

$$D_i = \sum_{k=0}^{N_s-1} d_{i,k} 2^{-i/2} \Psi(2^{-i}t - k), \tag{6}$$

and L, c_k, $d_{i,k}$, $\Phi(t)$, and $\Psi(t)$ are the number of levels of wavelet decomposition, scaling coefficients, detail coefficients, scaling function, and mother wavelet, respectively.

In the present study, Daubechies 12 and 20 filters are used for the wavelet decomposition technique of Mancinelli *et al.* [37] and the wavelet multiresolution analysis, respectively. The wavelet procedures are then carried out using Matlab.

III. RESULTS AND DISCUSSIONS

In this section, results on the spectral and statistical properties of flow fields as well as near- and far-field pressure signals are presented. The radiating sound and nonradiating pseudo-sound generated just behind the λ shocks, in the region of expansion fans, in the region of the fluctuating separated shear layers, and in the far field near the wake, are quantitatively analyzed and discussed. Wavelet multiresolution analysis of acoustic and hydrodynamic pressure fluctuations is performed to study the sound and pseudo-sound signatures associated with various scales of turbulent structures.

A. Near-field flow dynamics

Figure 3 shows the instantaneous streamwise velocity, vorticity magnitude, and dilatation fields around a circular cylinder at Re = 3900 and Ma = 0.9. As the flow passes through the upper and lower surfaces of the circular cylinder, it accelerates to form two corresponding supersonic zones.

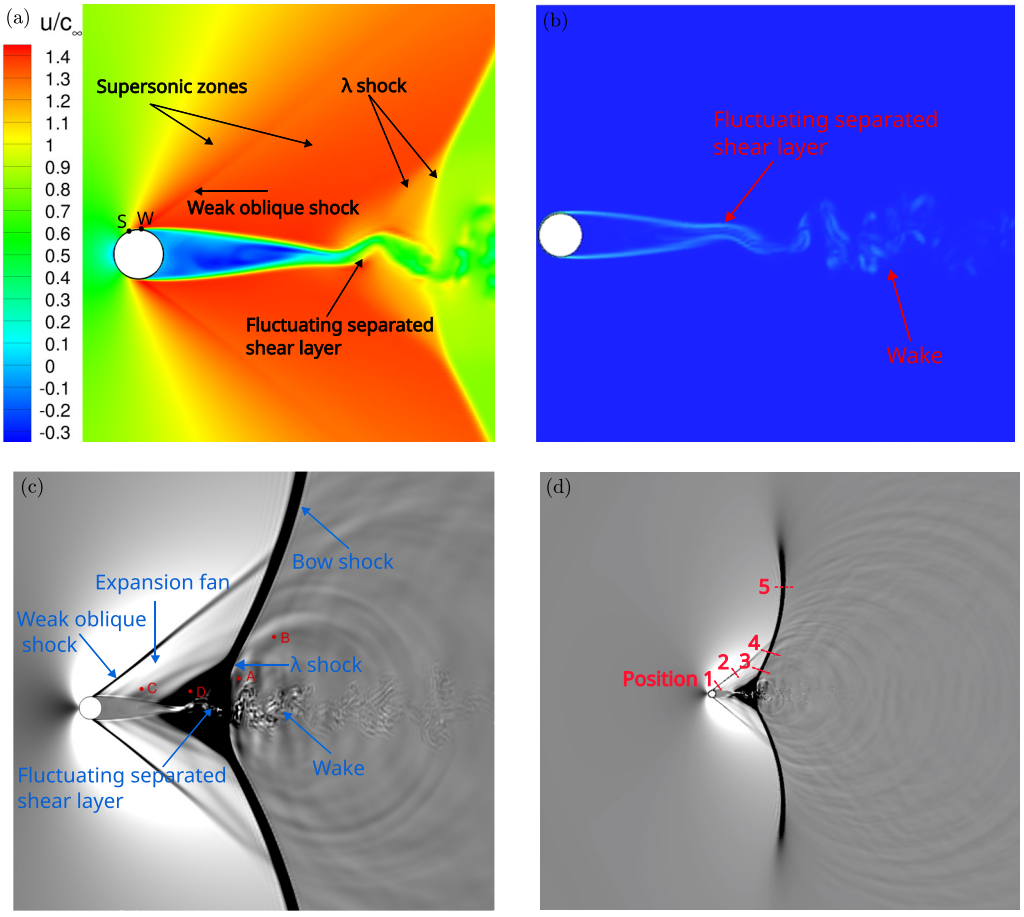

FIG. 3. Instantaneous flow fields of a circular cylinder at $\mathrm{Re} = 3900$ and $\mathrm{Ma} = 0.9$: (a) streamwise velocity; (b) vorticity magnitude with a contour level between 0 and $50c_\infty/D$; (c) dilatation in the near field; and (d) dilatation in both near and far fields with a contour level between $-0.1c_\infty/D$ and $0.1c_\infty/D$. Position S is where the flow becomes supersonic and W is the intersection between a weak oblique shock and the cylinder surface; positions A and B are in the region just behind the lambda (λ) shock; C and D are in the regions of the expansion fan and fluctuating separated shear layers, respectively. The flow quantities across the shocks at positions 1–5 in (d) are quantitatively assessed in this study.

Starting from position S on the cylinder surface in Fig. 3(a), the flow becomes locally supersonic. Two symmetric weak oblique shocks, one of which intersects the cylinder surface at position W, are formed due to the separation of the boundary layer on the cylinder surface. In fact, the separated shear layer and the cylinder surface form a compression corner and hence the weak oblique shock. The supersonic flows behind the weak oblique shocks are further redirected due to the inclined separated shear layers, forming two expansion fans within the two supersonic zones. Unsteady expansion waves are observed in the expansion fans, followed by unsteady compression waves that interact with the lambda (λ) shocks. Such interactions between expansion waves, compression waves, λ shocks, fluctuating separated shear layers, and the wake produce sound that propagates to the far field. Regarding the separated shear layers, at $x < 3D$, the supersonic flows stabilize the separated shear layers, and thus the separated shear layers become quasi-steady. From $3D < x < 6D$, the shear layer instability leads to the distortion and fluctuation of the separated shear layers, causing the flow to become unsteady. The two elongated separated shear layers incline towards the

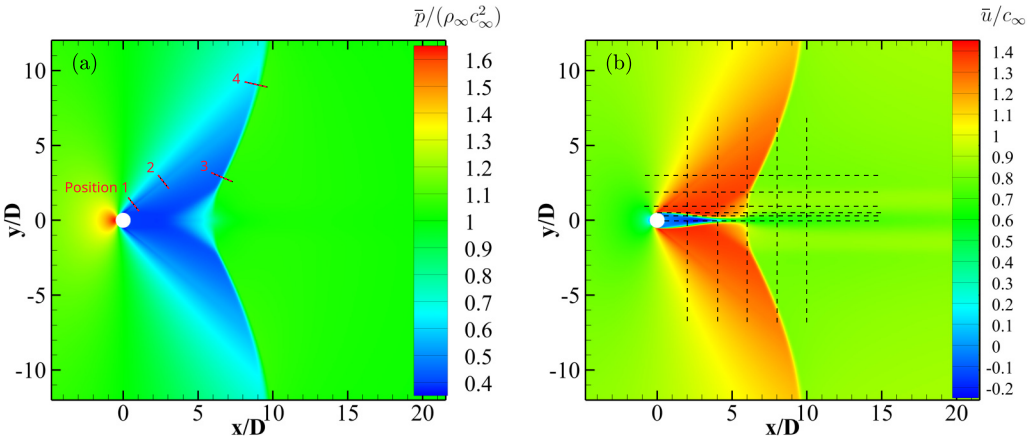

FIG. 4. Mean flow fields of (a) pressure and (b) streamwise velocity in the flow past a circular cylinder at Re = 3900 and Ma = 0.9. The dashed lines in (a) indicate the positions where flow quantities across shocks are assessed. Note that position 5, where the bow shock intersects the horizontal line at $y/D = 15$, is not shown here. In (b), the vertical dashed lines, from left to right, correspond to $x/D = 2$, 4, 6, 8, and 10, while the horizontal dashed lines, from bottom to top, correspond to $y/D = 0$, 0.35, 0.5, 1, 2, and 3.

cylinder centerline, narrowing the wake between them [Figs. 3(a) and 3(b)]. Figure 3(b) illustrates the instantaneous vorticity magnitude. Unlike in incompressible or subsonic conditions [3,4,18], at Ma = 0.9, the shear layer does not roll up to form a vortex, indicating that vortex shedding is indeed suppressed [24–27]. However, shear layer instabilities, manifested as fluctuations in the separated shear layers, are observed. While no roll-up of the shear layers occurs, the fluctuating shear layers are interrupted by λ shocks, forming the downstream wake. Due to the fluctuation of the separated shear layers, considerable sound is generated in the near field behind the separated shear layers and the λ shocks, and then propagates to the downstream far field [Figs. 3(c) and 3(d)]. Regarding the λ shocks, within $-1 < y/D < 1$, the two tails of each λ shock strongly interact with the fluctuating separated shear layers and the wake. Beyond this range, the λ shocks extend to the far field as quasi-steady bow shocks. These shock waves are formed in the downstream of the circular cylinder and hence do not attach to the cylinder surface. As a result, a nonlinear phenomenon arises, and the shock waves exhibit a bow shape. Regarding the turbulent wake, turbulent structures are generated between the two separated shear layers and convect downstream. The interaction between these structures and the λ shocks not only generates shock noise in the near field but also distorts the λ shocks due to pressure variations. The noise generation mechanism due to the interaction among various flow features makes the present study different from others on noise generation in compressible shear layers [60,61]. In Sec. III D, pressure fluctuation signals at positions A ($6.6D$, 170°) and B ($8.6D$, 160°) behind the fluctuating separated shear layers and the λ shocks are collected for analyses. In addition, in Sec. III E, pressure fluctuation signals at positions C ($2.5D$, 160°) and D ($4.6D$, 170°), one in the region of expansion waves and the other in the region of the fluctuating separated shear layers, are studied using wavelet analysis.

Figure 4 illustrates the mean pressure and streamwise velocity fields obtained from the present DNS. The supersonic zones generated by flow acceleration, combined with the recirculation zone, create a large low-pressure region. To quantitatively analyze the flow quantities in the directions perpendicular to both strong and weak shocks, the profiles of mean pressure, mean streamwise velocity, and instantaneous dilatation at five shock positions [see Figs. 3(d) and 4(a)] are presented in Fig. 5. As anticipated, there is a pronounced pressure increase and a sharp velocity decrease across the strong shock. For the weak shock, while the pressure and velocity jumps are steep at position 1, they become more moderate at position 2. The instantaneous dilatation profiles at the shock locations exhibit a characteristic "V" shape with minima observed in all five profiles at positions 1

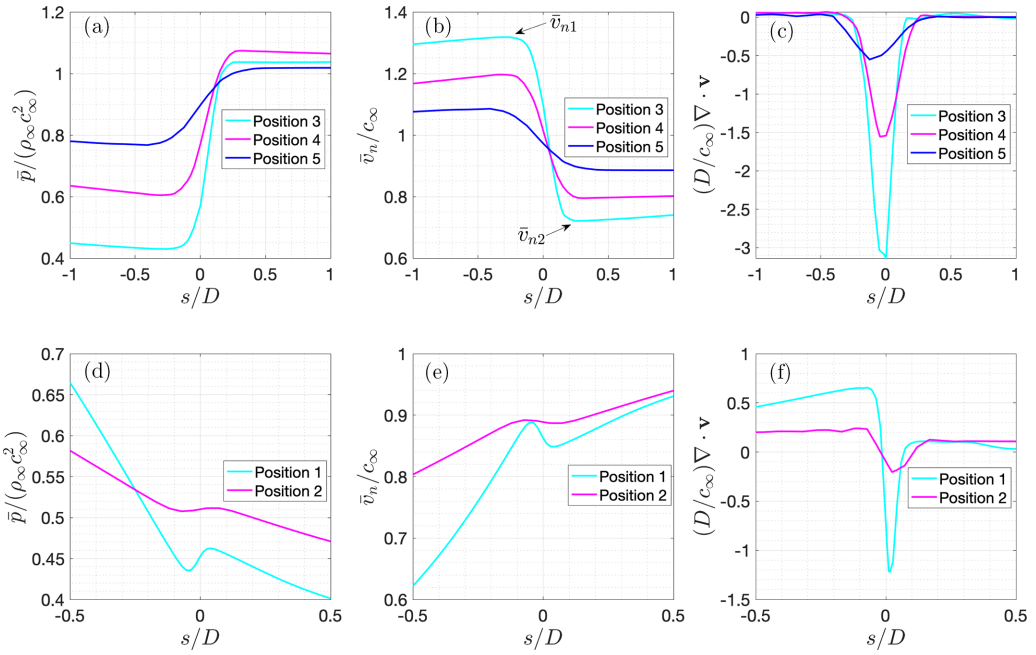

FIG. 5. Flow quantities are shown across the strong and weak shocks at positions 1–5: (a) mean pressure across the strong shock; (b) mean shock-normal velocity across the strong shock; (c) instantaneous dilatation across the strong shock; (d) mean pressure across the weak shock; (e) mean shock-normal velocity across the weak shock; and (f) instantaneous dilatation across the weak shock. The arrows of $\bar{v}_{n1}$ and $\bar{v}_{n2}$ in (b) respectively indicate the maxima and minima of the cyan curve for position 3.

through 5. For both weak and strong shocks, the minima increase, and the width of the V-shaped profile broadens as the position moves from the near field to the far field. It is worth noting that, in Fig. 5, the s coordinate for the pressure, shock-normal velocity, and dilatation profiles is defined such that $s = 0$ corresponds to the midpoint between the $\bar{v}_{n1}$ and $\bar{v}_{n2}$ coordinates.

Ida *et al.* [62] define the numerical shock thickness, δ_{shock}, for a one-dimensional (1D) stationary normal shock wave as follows:

$$\delta_{\text{shock}} = \frac{v_{n1} - v_{n2}}{\left|\frac{dv_n}{ds}\right|_{\max}}, \tag{7}$$

where v_n represents the shock-normal velocity, while the subscripts 1 and 2 indicate the preshock and postshock conditions, respectively. The numerator on the right-hand side denotes the velocity jump across the shock wave, whereas the denominator represents the maximum velocity gradient within the numerically diffused shock layer. To quantitatively evaluate the present shock thickness, Table I summarizes key parameters, including the preshock and postshock shock-normal mean velocities, the maximum gradient of the shock-normal mean velocity, mean shock thickness, and the ratios of mean pressure and density across the shocks at positions 1 to 5. For a Reynolds number of 3900 and a Mach number of 0.9, the cylinder diameter is approximately 193 μm under standard airflow conditions. The shock thickness at positions 1 to 5 is 9.1, 13.1, 39.8, 52.7, and 82.2 μm, respectively. In the region of the strong shock, the radial cell size is approximately 11 μm, providing four to seven grid points for resolving the strong shock segment between positions 3 and 5. As the weak oblique shock extends from the cylinder surface, the number of grid points for resolving the weak oblique shock varies: the near-wall region is resolved with many grid points, whereas fewer grid points are available in the relatively far-field region. The pressure ratio, a key indicator of shock

TABLE I. Flow quantities across the strong and weak shocks at positions 1–5 are presented. From left to right, the columns represent the positions of assessment, preshock shock-normal mean velocity, postshock shock-normal mean velocity, maximum gradient of the shock-normal mean velocity, mean shock thickness, mean pressure ratio across the shock, and mean density ratio across the shock.

Positions of assessment	$\bar{v}_{n1}/c_\infty$	$\bar{v}_{n2}/c_\infty$	$\lvert d\bar{v}_n/ds\rvert_{\max}(D/c_\infty)$	$\bar{\delta}_{\text{shock}}/D$	$\bar{p}_2/\bar{p}_1$	$\bar{\rho}_2/\bar{\rho}_1$
Position 1	0.888	0.849	0.835	0.047	1.062	1.044
Position 2	0.892	0.887	0.074	0.068	1.008	1.005
Position 3	1.318	0.721	2.899	0.206	2.412	1.840
Position 4	1.196	0.795	1.469	0.273	1.776	1.498
Position 5	1.085	0.886	0.467	0.426	1.327	1.223

strength, demonstrates that the strength of the strong shock (positions 3 to 5) is greater than that of the weak shock (positions 1 and 2). For both strong and weak shocks, the shock strength decreases progressively as the position moves from the near field to the far field.

Notably, the shock thickness calculated using Eq. (7) is smaller than the width of the V-shaped dilatation profiles. For instance, at position 3, the width of the V-shaped dilatation profile is approximately $0.45D$, which is significantly larger than the calculated shock thickness of $\bar{\delta}_{\text{shock}} = 0.206D$. This discrepancy indicates that, although the strong shock appears relatively thick in the dilatation contours [see Figs. 3(c) and 3(d)], it does not correspond to the shock thickness defined by Eq. (7). While the numerical thickness of the present shocks exceeds the analytical approximation provided by Puckett and Stewart [63], the shock thickness predicted by Eq. (7) is on the order of micrometers (less than 100 μm). This prediction is not far from the description by Kundu *et al.* [64], who describe a shock wave as a step-change compression sound wave with finite strength and a typical thickness on the order of micrometers. Furthermore, when comparing the dilatation or density gradient contours of similar studies [20,25,27], it is noteworthy that the current shock thickness aligns closely with that reported by Mani *et al.* [20] and is smaller than those reported in other studies [25,27].

The power spectral density (PSD) of the vertical velocity fluctuation at four near-field positions A, B, C, D and five different positions along the wake centerline is presented in Fig. 6. The calculation of the PSD of a signal is detailed in Appendix 1. It is evident that the peaks of the spectra occur at $\mathrm{St} = 0.4$, which represents the fluctuating frequency of the separated shear layers, for probes positioned both on the centerline and off the centerline. At higher frequencies, harmonics are observed. Along the wake centerline, the spectrum levels at $x/D = 5.0$, 6.6, and 8.7 are higher

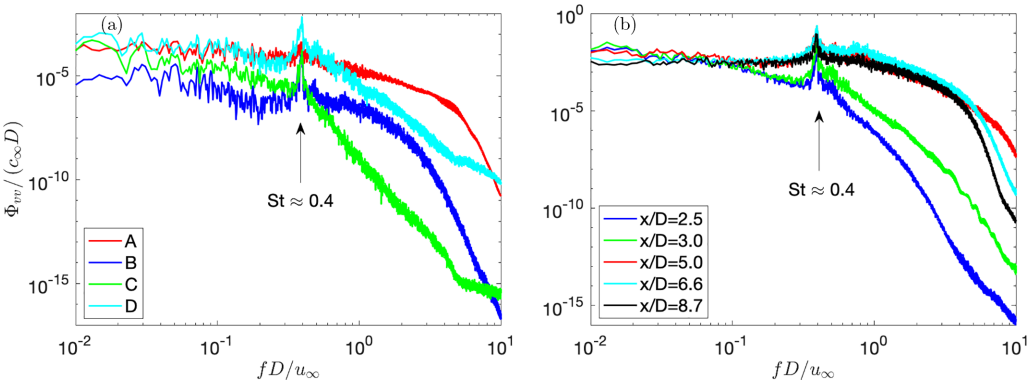

FIG. 6. The PSD of the vertical velocity fluctuation with a dominant peak around $\mathrm{St} = fD/u_\infty = 0.4$ at (a) four near-field positions A, B, C, and D and (b) five positions on the wake centerline.

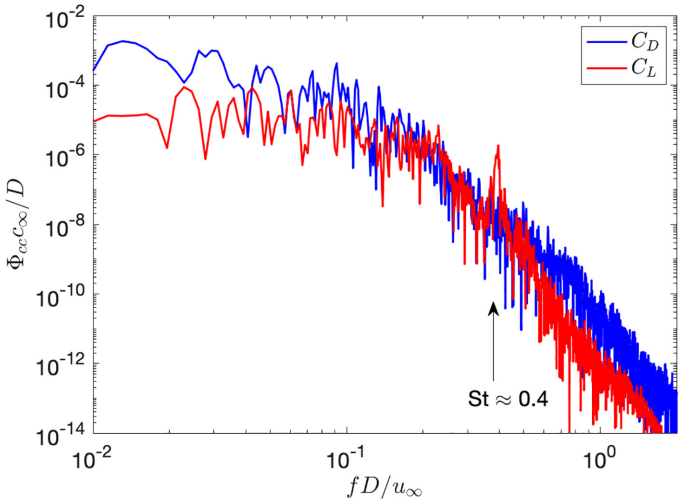

FIG. 7. The PSD of drag and lift coefficients.

because these positions fall within or are close to the region of the fluctuating separated shear layers. The fluctuating frequency of the separated shear layers, with a Strouhal number of St ≈ 0.4, is confirmed by the PSD of the lift coefficient, as shown in Fig. 7 alongside the PSD of the drag coefficient. The lift coefficient demonstrates a distinct peak at St ≈ 0.4. Since the lift is a result of the pressure on the cylinder surface, it is expected that the peak frequency of the lift coefficient is the same as the peak frequency of the wall pressure spectra, which will be shown subsequently. Additionally, it is evident that the drag coefficient carries more energy than the lift coefficient at frequencies outside of St ≈ 0.4.

Figure 8 compares the present wall pressure coefficient and root-mean-square pressure fluctuation on the cylinder surface with those obtained from the CLES at Re = 40 000 and Ma = 0.9 by Xia *et al.* [27]. The reference CLES at Re = 40 000 and Ma = 0.9 was chosen due to a lack of experimental and simulation data in the literature. Considering that a transonic cylinder flow at Ma < 0.9 differs significantly from one at the critical Mach number of 0.9 [24–27], it is essential to select a reference case with the exact Mach number, even if the Reynolds number differs slightly. Additionally, in circular cylinder flows, both Re = 3900 and Re = 40 000 remain within

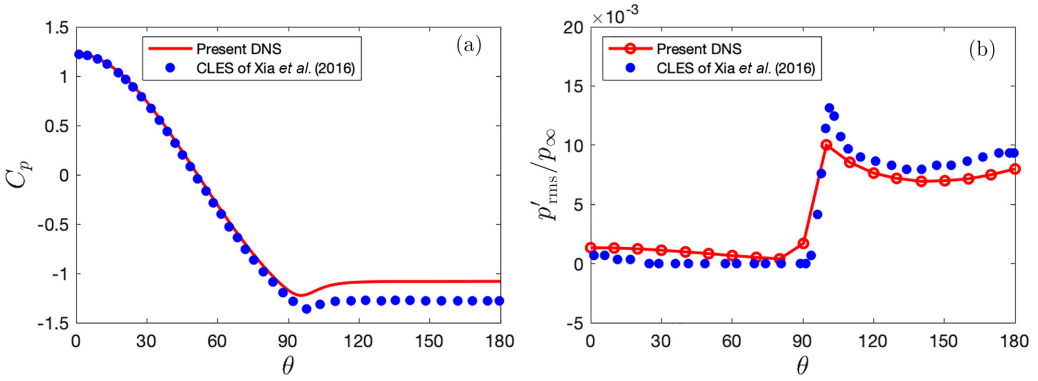

FIG. 8. Comparison of (a) pressure coefficients and (b) root-mean-square pressure fluctuations on the cylinder surface at the same Mach number (Ma = 0.9) between the present DNS at Re = 3900 and the CLES of Xia *et al.* [27] at Re = 40 000.

TABLE II. Comparison of flow quantities at three different Mach numbers. The columns, from left to right, represent the Mach number, drag coefficient, base pressure coefficient, and minimum averaged streamwise velocity. All cases have a Reynolds number of 3900.

Case	Ma	C_d	$-C_{\text{pbase}}$	$u_{\min}/u_\infty$
Present DNS	0.9	1.69	1.08	−0.29
DNS [31]	0.4	1.21	1.13	−0.38
DNS [31]	0.2	1.04	0.94	−0.44

the subcritical regime, meaning that the results should be comparable as long as the Mach number is held constant. The results show that C_p decreases from the front stagnation point until it reaches a minimum value between 90° and 100°. In the region of favourable pressure gradient, despite a difference in Reynolds numbers by an order of magnitude, the present DNS prediction of C_p agrees well with that obtained in the CLES of Xia *et al.* [27]. Beyond the minimum, C_p shows a slight increase, then remains stable up to the rear base point. However, in the region of adverse pressure gradient and flow separation, the pressure coefficient in the present DNS is higher than that in CLES, a trend similarly noted in the comparison of C_p between DNS and LES of cylinder flows at Ma = 0.2 [31]. Regarding the root-mean-square pressure fluctuation, the present DNS is in reasonable agreement with the CLES, with a slight deviation. The quality of the present DNS is showcased by the energy spectra presented in Appendix 2. Given that p'_{rms}/p_∞ is on the order of 10^{-3}, the difference between the present DNS and the referenced CLES results is minor. This discrepancy may be attributed to variations in simulation strategies, numerical schemes, Reynolds numbers, and other factors.

Table II presents a comparison of the drag coefficient, base pressure coefficient, and minimum averaged streamwise velocity between the current simulation (Ma = 0.9) and existing simulations at lower Mach numbers (Ma = 0.2 and 0.4) [31]. As expected, the drag coefficient increases significantly with Mach number. Additionally, the minimum averaged streamwise velocity also increases with Mach number, indicating a reduction in reverse flow as compressibility rises. However, the base pressure shows minimal variation as the Mach number increases from 0.4 to 0.9, suggesting that the higher drag observed at Ma = 0.9 primarily results from increased pressure on the windward side of the cylinder.

Figure 9 compares the mean streamwise velocity along various horizontal lines ($0 \leqslant y/D \leqslant 3$), as represented by the horizontal dashed lines in Fig. 4(b). Along the wake centerline ($y/D = 0$), a recirculation region exists with a strong reversing flow until $x/D = 4$, beyond which the flow accelerates towards the downstream due to the narrower wake region caused by the converging separated shear layers [see also Figs. 3(a) and 4(b)]. The wake velocity reaches a local maximum at $x/D = 5.5$ where the wake passage is the narrowest. At $5.5 < x/D < 6.3$, the wake flow decelerates due to the wider wake passage between the two separated shear layers. Further downstream, as the wake flow goes behind the separated shear layers, its velocity recovers gradually. Along other horizontal lines ($0.35 \leqslant y/D \leqslant 3$), the velocity increases due to entering the locally supersonic region, and decreases due to exiting the supersonic region. The curves with a sharp decrease of velocity indicate crossing the shocks. Figure 10 shows the mean and variance of streamwise and vertical velocities along different vertical lines ($2 \leqslant x/D \leqslant 10$), as marked by the vertical dashed lines in Fig. 4(b). Overall, velocities are more protruding in the narrow wake passage. Turbulence is mainly generated in the narrow wake passage.

B. Far-field sound propagation

Figure 11 shows the PSD of pressure fluctuations at four far-field positions ranging from 140° to 170°, as indicated by the blue probes in Fig. 2. The PSD is computed at each sampled position and averaged in the spanwise direction. It is clear that all four spectra have a peak value around

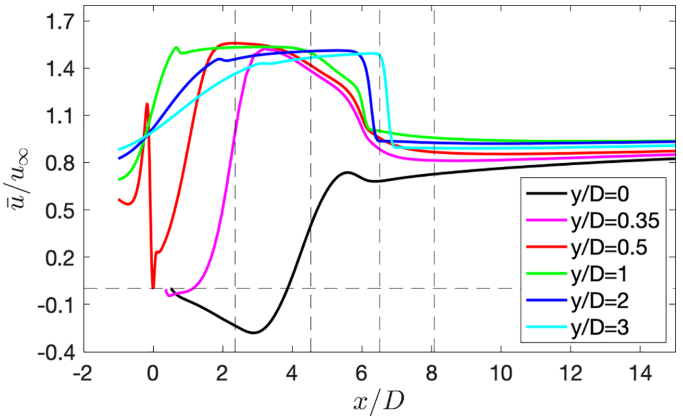

FIG. 9. Comparison of mean streamwise velocity along different horizontal lines in the wake region. The horizontal dashed line represents $\bar{u}/u_\infty = 0$. From left to right, the four vertical dashed lines [passing through the probes C, D, A, and B in Fig. 3(c), respectively] correspond to $x_C/D = 2.35$, $x_D/D = 4.53$, $x_A/D = 6.5$, and $x_B/D = 8.08$. Note that the center axis of the circular cylinder is located at the origin of the coordinate system.

St = 0.4, which is the fluctuating frequency of the separated shear layers. In addition, a valley of spectra is observed between St = 0.16 and 0.17. It remains unclear whether this arises from destructive interference mechanisms. Unlike the subsonic cases [12,65,66], where far-field sound

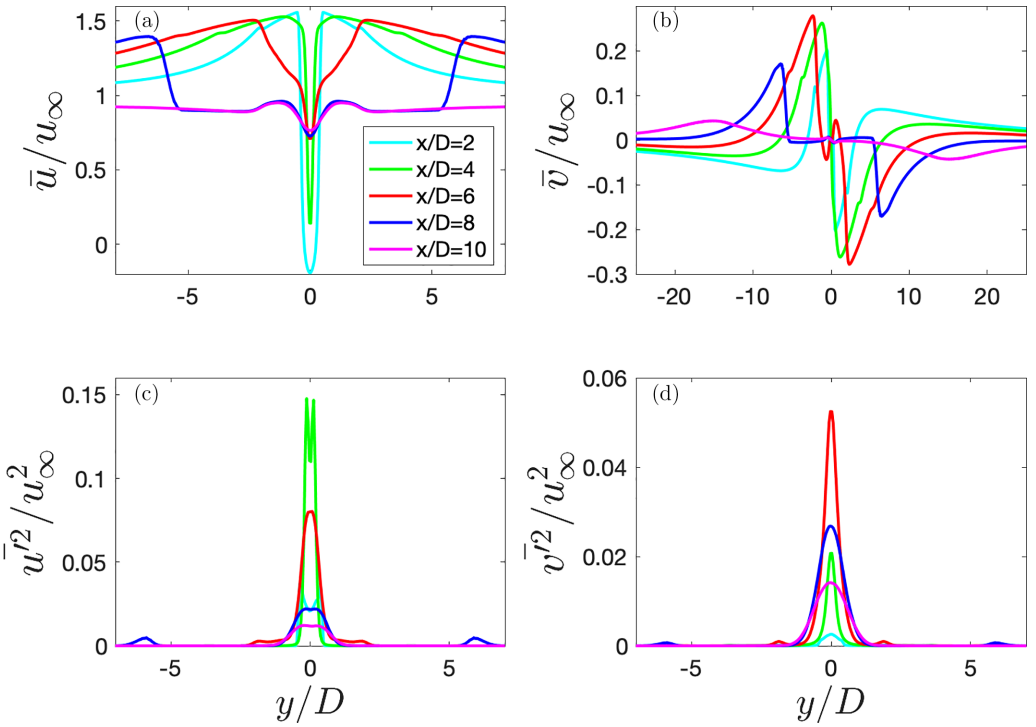

FIG. 10. Comparison of the mean and variance of streamwise and vertical velocities along different vertical lines across the wake region.

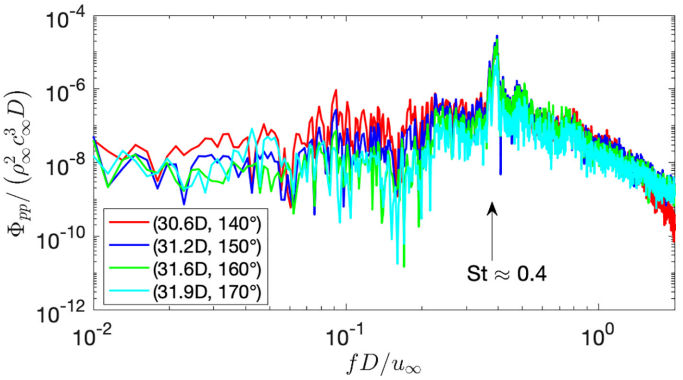

FIG. 11. The PSD of pressure fluctuations at four far-field positions with the same dominant peak at St = 0.4.

exhibits a dominant frequency at St = 0.2, no spectral peak at St = 0.2 is observed in the present case. This suggests that the dominant sound field generated by a circular cylinder under the present transonic condition fundamentally differs from that under subsonic conditions. The quadrupoles, rather than dipoles, dominate the sound field in the present condition [67].

Figure 12 shows the sound pressure level (SPL) directivities at four discretized frequencies: St = 0.2, 0.4, 0.47, and 0.74. The SPL is defined as

$$\mathrm{SPL} = 10\log_{10}\left(\frac{\Phi_{pp}\Delta f}{p_{\mathrm{ref}}^2}\right), \tag{8}$$

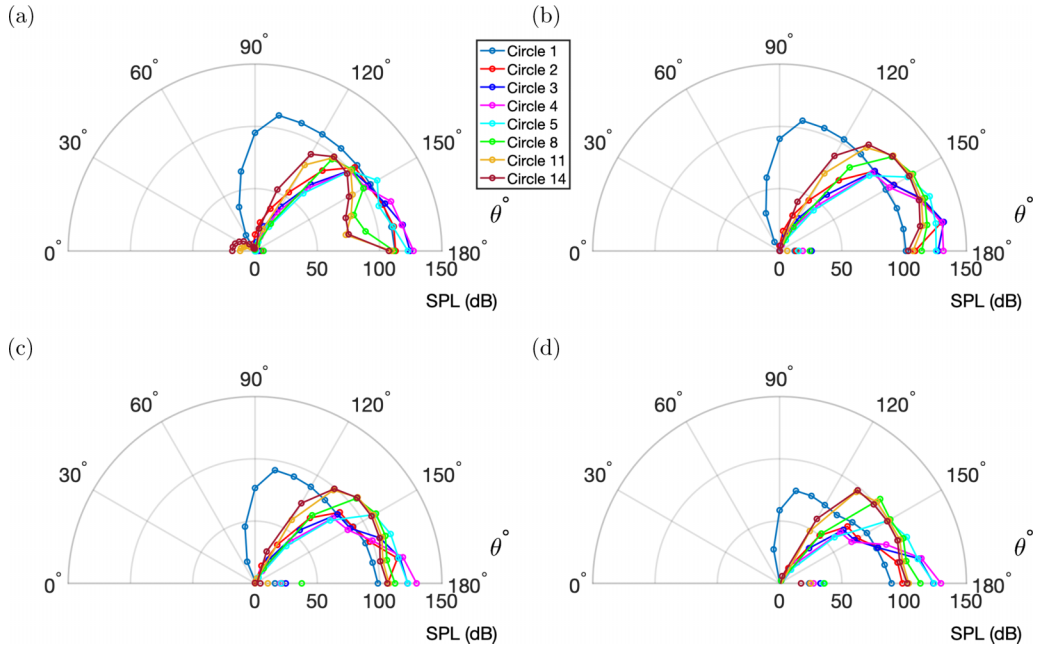

FIG. 12. Directivities of the SPL at different frequencies: (a) St = 0.2, (b) St = 0.4, (c) St = 0.47, and (d) St = 0.74.

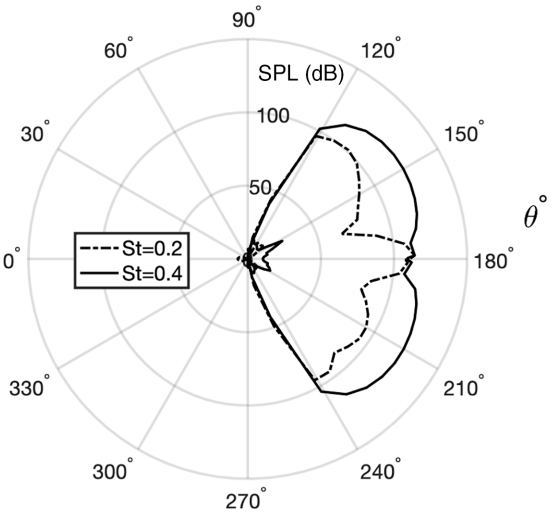

FIG. 13. Directivities of the SPL along a circle centered at $(3.3D, 180^\circ)$ with a radius of $16.8D$ at $\mathrm{St} = 0.2$ and $\mathrm{St} = 0.4$.

where Φ_{pp} is the PSD and $p_{\mathrm{ref}} = 2 \times 10^{-5}$ Pa represents the reference pressure. As shown in Fig. 12, the SPL decreases dramatically from 120° to 110° because the bow shock waves act as noise barriers, preventing sound from propagating upstream [see Figs. 3(c) and 3(d)], consistent with findings by Tamura and Tsutahara [28]. The reason why the bow shocks act as noise barriers is that the flow upstream of the bow shocks is locally supersonic, indicating that the flow speed is larger than the propagating speed of sound waves. In the upstream of the bow shock waves, the SPL is significantly lower, thereby making the upstream region a region of "silence". In the downstream of the bow shock waves, the SPL is high at all four frequencies, with the one at $\mathrm{St} = 0.4$ being the highest. In the SPL directivity of $\mathrm{St} = 0.4$, the highest SPL is observed in the sectorial region between 150° and 180°. It appears that the major sound sources are located within this sectorial region. For this reason, in the sections that follow, the pressure fluctuations in this region, for example, at sampling positions A, B, C, and D, will be examined and analyzed in detail. It should be noted that, although the SPL on the cylinder surface (i.e., circle 1) is high, particularly at $\theta < 120^\circ$, the pressure fluctuations on the cylinder surface are still much weaker in comparison to those in the sectorial region between 150° and 180°, considering that the SPL is a logarithmic quantity. As the radial distance from this region increases, the SPL decreases due to the decaying of the propagating sound waves.

In order to gain a better understanding of sound propagation in different directions and a better visualization of sound propagation blocked by the bow shocks, pressure signals are sampled at probes densely distributed on a circle centered at $(3.3D, 180^\circ)$ with a radius of $16.8D$. The corresponding far-field SPL directivities at $\mathrm{St} = 0.2$ and 0.4 are shown in Fig. 13. In contrast to subsonic regimes, where sound pressure directivities exhibit doublet-like shapes [11,12,14], the directivities under the present condition have significantly higher pressure levels in the downstream region and much lower levels in the upstream region. This is because quadrupole noise plays a more important role than dipole noise at this Mach number [67]. At both $\mathrm{St} = 0.2$ and $\mathrm{St} = 0.4$, abrupt changes in SPL are found at 120° and 240°, which correspond to the bow shock waves as shown in Fig. 3.

C. Correlation of far-field pressure fluctuations with both cylinder wall and near-wake pressure fluctuations

Figure 14 presents the PSD of pressure fluctuations at five different positions around the circumference of the cylinder. It is observed that all five spectra exhibit a similar trend. The spectra

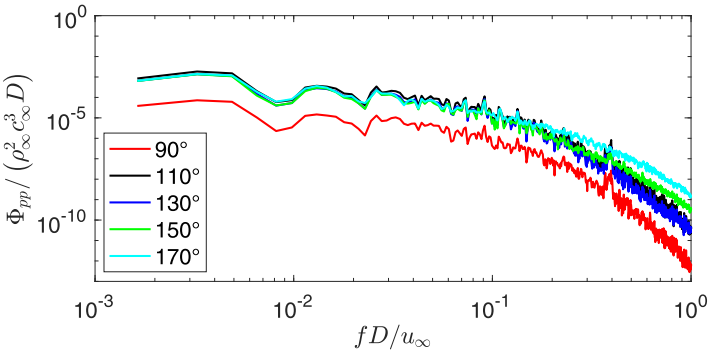

FIG. 14. The PSD of pressure fluctuations at five locations on the cylinder surface.

remain flat at low frequencies (St < 0.1). But at higher frequencies, they exhibit a steady decline, with a subtle peak observed at St $= 0.4$ across all spectra except for the one at $\theta = 170^\circ$. The PSD level at this peak is modest and falls below the PSD levels at frequencies under St < 0.2. Figure 15 shows the PSD of pressure fluctuations at four positions, A, B, C, and D, in the near wake behind the cylinder. Positions A and B are located behind the λ shocks, position C is in the region of the expansion fan, and position D is in the region of the fluctuating separated shear layers. A prominent peak is observed in all four spectra. The spectra from probes A and D are generally higher, as these probes are closer to the fluctuating separated shear layers (Fig. 3).

To further identify the sound sources in the near field of the cylinder, the correlation between far-field pressure fluctuations and either cylinder wall pressure fluctuations or near-wake pressure fluctuations is evaluated. Figure 16 compares the cross-correlation between a far-field pressure fluctuation signal at $(31.6D, 160^\circ)$ and near-field pressure fluctuation signals at probes A, D, and five wall probes ranging from $\theta = 90^\circ$ to 170°. Probes A, D, and the wall probe $(0.5D, 170^\circ)$ are situated on the $\theta = 170^\circ$ radial line. The results indicate that the pressure fluctuations at positions A and D are more strongly correlated with the far-field pressure fluctuations, whereas the correlation between wall pressure fluctuations and far-field pressure fluctuations is very weak. Since the correlation between the far-field pressure fluctuation and the pressure fluctuations at the five wall probes ($\theta = 90^\circ$, 110°, 130°, 150°, and 170°) falls within the range of $[-0.1, 0.1]$, it is very low, indicating that wall pressure fluctuations are uncorrelated with the far-field pressure fluctuation. This suggests that the sound source is not located on the cylinder surface but rather in the near wake. The sound originates in the near wake and passes through probes A and D, leading to a good correlation between the pressure fluctuations at these probes and the far-field pressure fluctuation.

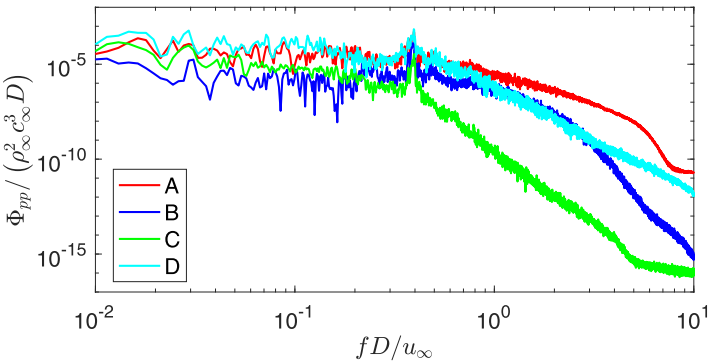

FIG. 15. The PSD of pressure fluctuations at four different positions in the near wake behind the cylinder.

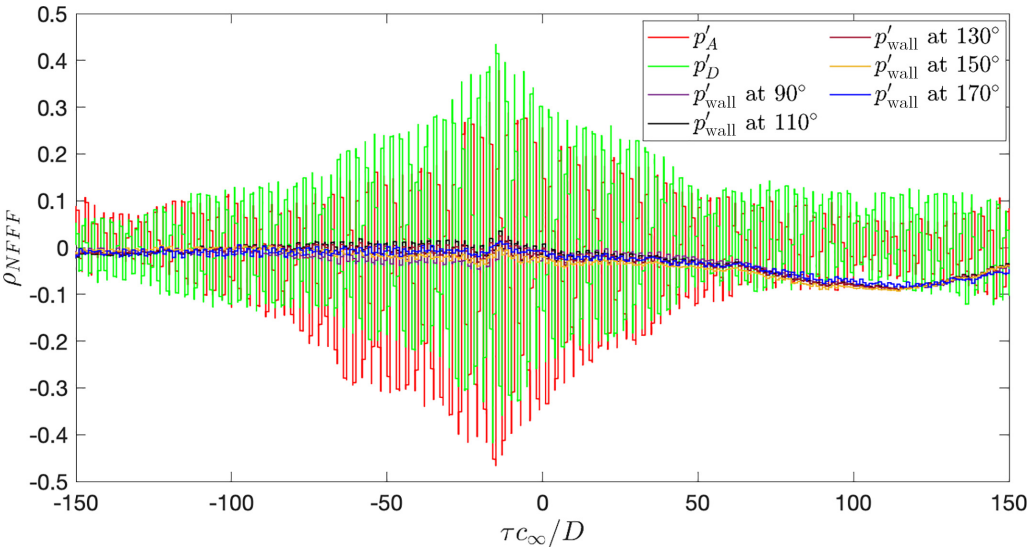

FIG. 16. Comparison of cross correlation between a far-field pressure fluctuation signal and near-field pressure fluctuation signals at A, D, and five wall probes ranging from $\theta = 90^\circ$ to 170°.

The propagating capabilities of these pressure fluctuations will be further evaluated using a wavelet decomposition technique [37] and multiresolution analysis.

D. Wavelet decomposition of near-field pressure fluctuations just behind the λ shocks

In order to quantitatively assess the sound and pseudo-sound in the near field, here the radiating component of near-field pressure fluctuations is isolated from the nonradiating component. Two instantaneous pressure fluctuation signals at positions A and B just behind the λ shocks are decomposed into acoustic and hydrodynamic components using the aforementioned wavelet decomposition technique [37], as described in Sec. II C. Figure 17 shows variations of the acoustic and hydrodynamic cross-correlation coefficient peaks between either the near-field separated acoustic or hydrodynamic component and three far-field pressure fluctuations. It is evident that the acoustic cross-correlation coefficient peaks increase gradually until they reach the maximum after which they diminish as the threshold decreases by 1% after each iteration. At the optimal iterations, the cross-correlation coefficient peaks between the acoustic and far-field pressure fluctuations are at a higher level than the ones between the hydrodynamic and far-field pressure fluctuations, as a result of the fact that acoustic pressure fluctuations radiate to the far field and thus correlate well with the far-field sounds whereas hydrodynamic pressure fluctuations do not radiate to the far field. Although the cross-correlation levels are somewhat different because of a different selection of far-field pressure fluctuations for the wavelet decomposition procedure, it has to be noted that the maximum values of all the acoustic cross-correlation coefficient peaks are reached around the 84th iteration at which the threshold is selected for the wavelet decomposition. In other words, the wavelet decomposition procedure is independent of the selection of far-field pressure fluctuations. In the following decomposition procedures, the far-field position $(31.6D, 160^\circ)$ is selected.

Figure 18 shows the PSD of the near-field pressure fluctuations and their separated acoustic and hydrodynamic components at positions A and B just behind the λ shocks. At position A, the hydrodynamic pressure fluctuation dominates over the acoustic one at most frequencies, with the disparity being larger in the frequency range $\mathrm{St} > 0.5$. At the fluctuating frequency of the separated shear layers ($\mathrm{St} = 0.4$), the acoustic pressure fluctuation dominates over the hydrodynamic one.

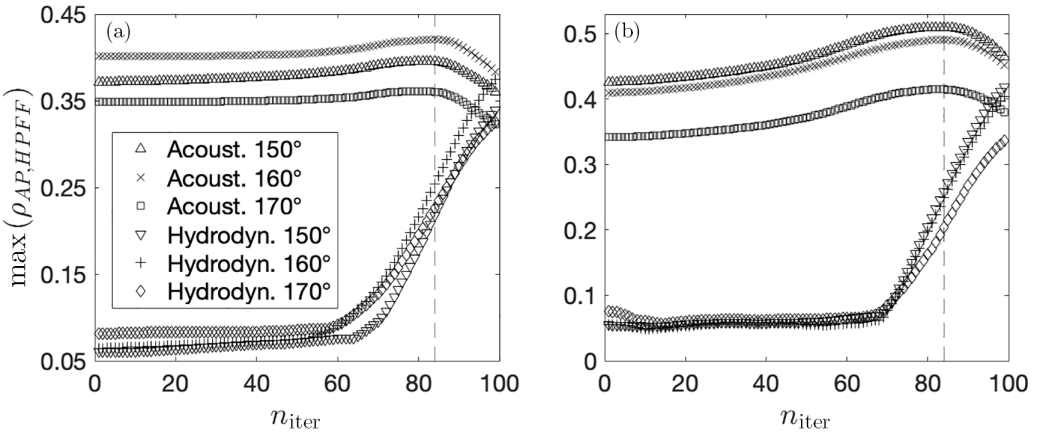

FIG. 17. Cross-correlation coefficient peaks between the far-field pressure fluctuation at three different locations and the near-field separated acoustic (hydrodynamic) component at positions (a) A (6.6D, 170°) and (b) B (8.6D, 160°). "Acoust." represents acoustic cross-correlation coefficient peak and "Hydrodyn." represents hydrodynamic cross-correlation coefficient peak. The angles 150°, 160°, and 170° represent that the p_{FF} is selected at (31.2D, 150°), (31.6D, 160°), and (31.9D, 170°), respectively. The iteration at which the threshold is selected for the wavelet decomposition procedure is highlighted with a vertical dashed line.

Thus, the pressure fluctuation at position A consists more of nonradiating pseudo-sound and less of radiating sound at most frequencies, while the situation is inverse at the fluctuating frequency of the separated shear layers. At position B, it is evident that the acoustic pressure fluctuation dominates over the hydrodynamic one at most frequencies including the fluctuating frequency of the separated shear layers. This is because position B is situated in a direction perpendicular to the wake and is relatively distant from the fluctuation of the separated shear layers. The hydrodynamic pressure fluctuations generated in the nearby field decay rapidly along the wake-perpendicular direction as the distance from this region increases [50].

Figure 19 shows the kernel density estimated probability density function (PDF) of the near-field pressure fluctuations and their separated acoustic and hydrodynamic components at positions A and B. Given that the present variables are in a wide range while most values are concentrated

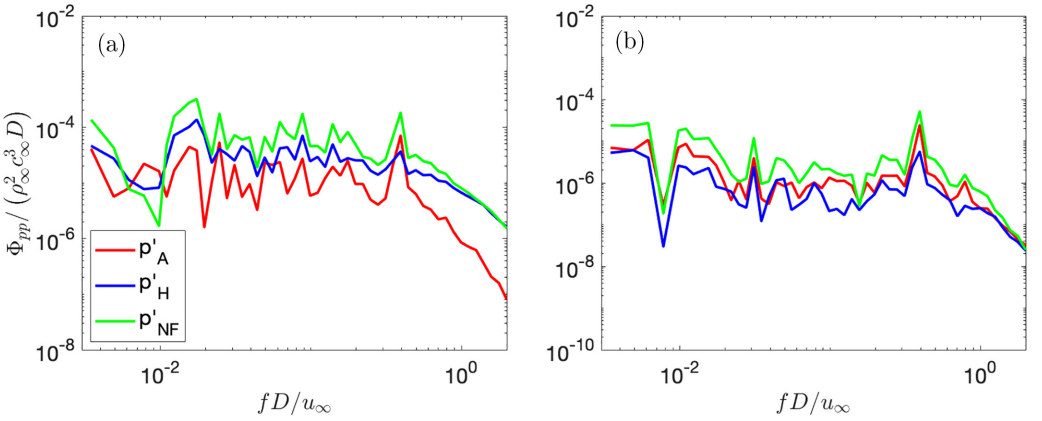

FIG. 18. The PSD of the near-field pressure fluctuations and their separated acoustic and hydrodynamic components at positions (a) A (6.6D, 170°) and (b) B (8.6D, 160°). The spectra are bin averaged over 1/6 octave. A Hann window is adopted to avoid spectral leakage.

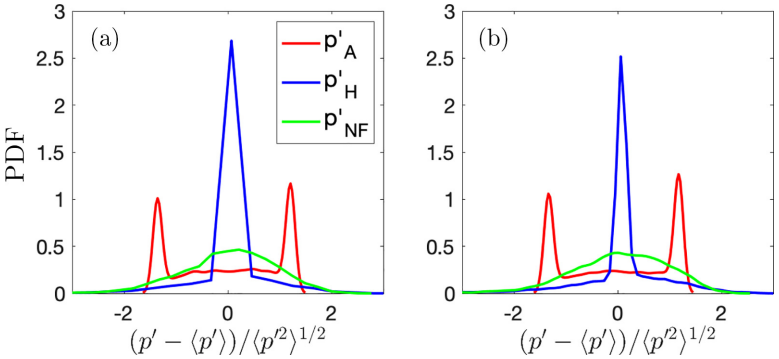

FIG. 19. The kernel density estimated PDF of the near-field pressure fluctuations and their separated acoustic and hydrodynamic components at positions (a) A ($6.6D$, 170°) and (b) B ($8.6D$, 160°).

around some specific values (e.g., the origin), neither large nor small bins are appropriate for the histogram. Here the kernel density estimation (KDE) produces smooth estimate of the PDF. Two important parameters of the nonparametric KDE are the kernel type and the bandwidth which influence the smoothness of the resulting distribution. In the present analysis, the KDE adopts a Gaussian kernel and a bandwidth based on the minimization of the mean integrated squared error [68]

$$h = \sigma(4/3)^{(1/5)} N_s^{(-1/5)}, \tag{9}$$

where σ is the standard deviation of the pressure fluctuation time series. According to Fig. 19, at both positions A and B, the normalized hydrodynamic pressure fluctuations have a single peak around zero whereas the normalized acoustic pressure fluctuations have two peaks, one on the negative and the other on the positive axis. For the hydrodynamic pressure fluctuations, the single peak around zero is an evidence of the intermittent nature of hydrodynamic pressure fluctuations. This is because largest possibility around zero suggests that there is no hydrodynamic pressure fluctuations during much of the time. For the acoustic pressure fluctuations, the two distinct peaks in the PDF are evidences of the propagating acoustic waves: the pressure fluctuations switch to positive and negative values whose magnitudes are nearly the same. These peaks in the PDF are related to the dominant tone of the acoustic pressure fluctuation at the fluctuating frequency of the separated shear layers. The stronger the tone, the further these peaks will be from the origin.

E. Wavelet decomposition of pressure fluctuations in the regions of expansion fans and fluctuating separated shear layers

In this subsection, the pressure fluctuations at two near-field positions, one in the region of expansion fans and the other in the region of the fluctuating separated shear layers, are decomposed through the same procedures as described in the Sec. III D.

Figure 20 shows the PSD of near-field pressure fluctuations and their separated acoustic and hydrodynamic components at positions C and D. At position C in the region of expansion fans, the hydrodynamic pressure fluctuation is weak compared to the dominant acoustic pressure fluctuation across the entire frequency range, meaning the pressure fluctuation is nearly acoustic. This is probably because, at position C in the region of expansion fans, the flow has not yet become turbulent. For the acoustic component, although a local peak of the PSD of acoustic component at $\mathrm{St} = 0.4$ still occurs, the magnitude of the PSD is much larger at lower frequencies (i.e., $\mathrm{St} < 0.1$). Thus, pressure waves in the region of expansion fans are principally low-frequency acoustic waves.

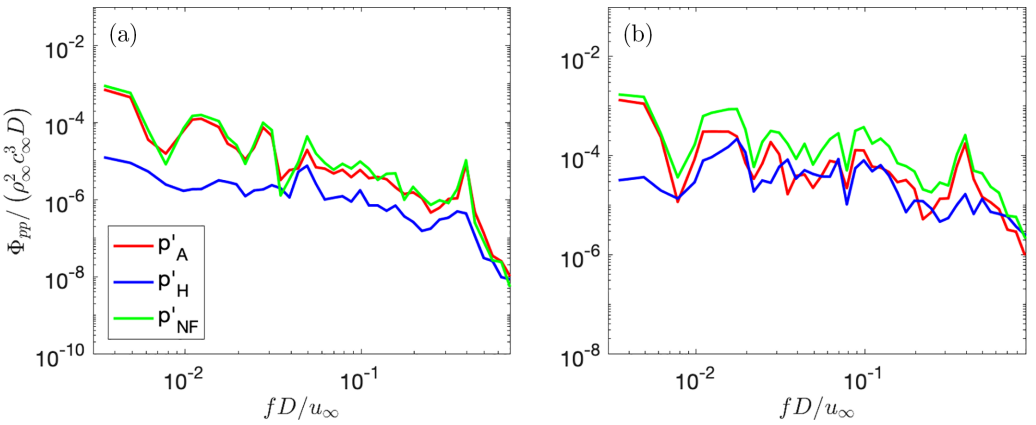

FIG. 20. The PSD of the near-field pressure fluctuations and their separated acoustic and hydrodynamic components at positions (a) C ($2.5D$, 160°) and (b) D ($4.6D$, 170°). The spectra are bin-averaged over 1/6 octave. A Hann window is adopted to avoid spectral leakage.

At position D in the region of the fluctuating separated shear layers, the acoustic and hydrodynamic pressure fluctuations show comparable strengths at most frequencies except at the lowest frequencies and the frequency of the fluctuating separated shear layers. At the frequency of the fluctuating separated shear layers (St = 0.4), the radiating acoustic component dominates over the nonradiating hydrodynamic counterpart. This is clearly reflected in Figs. 12(b) and 13, where the pressure fluctuation level remains very high in the downstream far field due to the strong radiation of the acoustic component. It is thus clear that, although the pressure fluctuation at position D consists of comparable amount of radiating acoustic sound and nonradiating hydrodynamic pseudo-sound at most frequencies, it mainly consists of radiating acoustic sound at the fluctuating frequency of the separated shear layers. In addition, the level of acoustic pressure fluctuation is higher at position D than at positions A, B, and C, suggesting that sound pressure waves are generated primarily by the fluctuation of the separated shear layers.

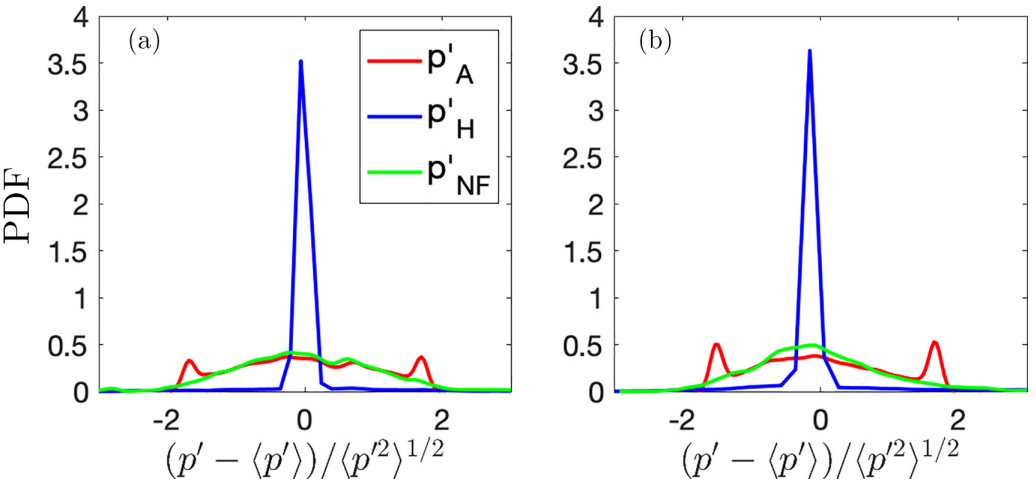

FIG. 21. The kernel density estimated PDF of the near-field pressure fluctuations and their separated acoustic and hydrodynamic components at positions (a) C ($2.5D$, 160°) and (b) D ($4.6D$, 170°).

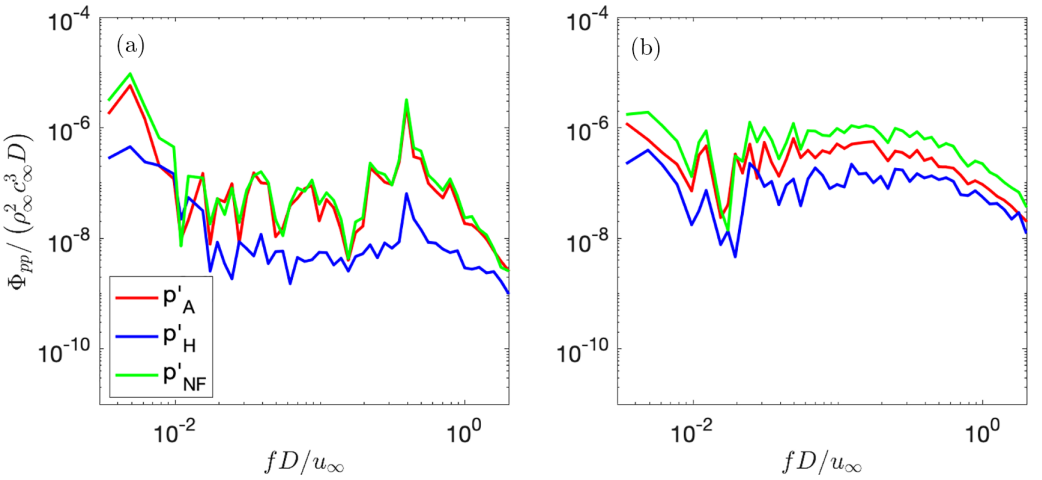

FIG. 22. The PSD of the far-field pressure fluctuations and their separated acoustic and hydrodynamic components at positions (a) E (20.9D, 170°) and (b) F (32D, 180°). The spectra are bin averaged over 1/6 octave. A Hann window is adopted to avoid spectral leakage.

Figure 21 presents the kernel density estimated PDF of the near-field pressure fluctuations and their separated acoustic and hydrodynamic components at positions C and D. At both positions, the hydrodynamic pressure fluctuation exhibits a single peak of PDF around zero. These peaks are higher than those at positions A and B because the intermittent hydrodynamic pressure fluctuations occur less frequently at these locations than in the highly turbulent near-field region behind the λ shocks. In addition, it is found that the PDF distribution of acoustic pressure fluctuations are flatter and the two peaks are further away from the origin at positions C and D than at positions behind the λ shocks. This is because the low-frequency components of the acoustic pressure fluctuation signals at both C and D are more energetic than the high-frequency components, as also demonstrated by the PSD of acoustic pressure fluctuations in Fig. 20. In other words, the more energetic components occur less frequently, which results in further and shorter peaks of the PDF of the acoustic pressure fluctuations.

F. Wavelet decomposition of pressure fluctuations in the far field near the wake

In this subsection, in order to investigate how the wake turbulence affects the acoustic and hydrodynamic pressure fluctuations in the far field, the pressure fluctuations at two far-field positions within or near the wake, one located at probe E (20.9D, 170°) and the other at probe F (32D, 180°), are decomposed using the same wavelet procedures.

Figure 22 shows the PSD of the far-field pressure fluctuations and their separated acoustic and hydrodynamic components at positions E and F. At position E, it is observed that the acoustic pressure fluctuation dominates over the hydrodynamic counterpart, due to the fact that the wake passage is narrow, and that position E is located outside the wake passage. At position F, compared to the hydrodynamic pressure fluctuation, the acoustic pressure fluctuation still prevails, particularly at low to middle frequencies. This is because the wake turbulence decays significantly along such a long distance from the downstream near field to position F, as also evidenced in Appendix 2. It is thus clear that, in the far cylinder wake, the pressure fluctuations are not significantly affected by the wake hydrodynamics. However, in the near cylinder wake, the pressure fluctuations are strongly affected by the wake hydrodynamics, as shown in Fig. 18.

Figure 23 shows the kernel density estimated PDF of the near-field pressure fluctuations and their separated acoustic and hydrodynamic components at positions E and F. The distributions are similar

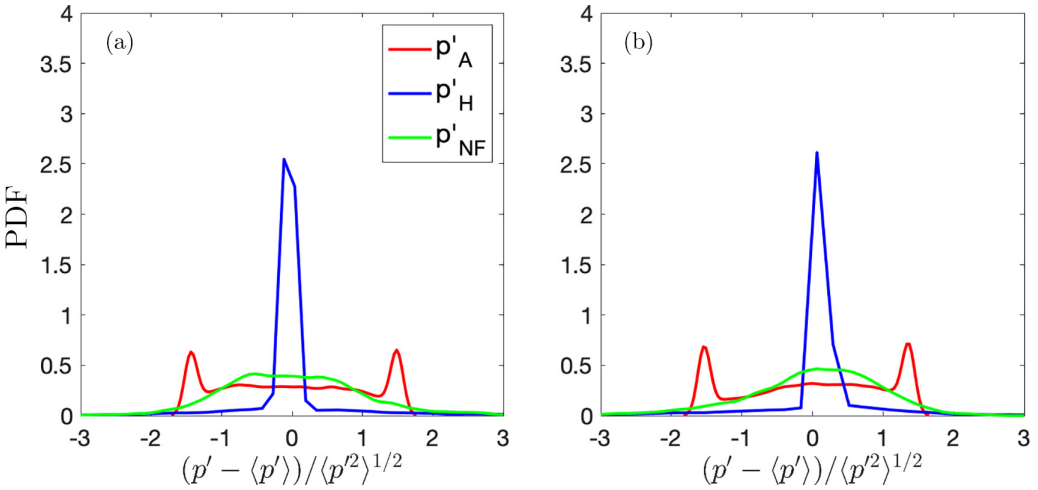

FIG. 23. The kernel density estimated PDF of the far-field pressure fluctuations and their separated acoustic and hydrodynamic components at positions (a) E (20.9D, 170°) and (b) F (32D, 180°).

to those in Figs. 19 and 21, with a single peak of the hydrodynamic pressure fluctuations and two peaks of the acoustic pressure fluctuations.

G. Wavelet multiresolution analysis of acoustic and hydrodynamic pressure fluctuations

In order to quantitatively assess the sound and pseudo-sound signatures associated with different scales of turbulent structures, the acoustic and hydrodynamic pressure fluctuations at position A in the region just behind the λ shocks and position D in the region of the fluctuating separated shear layers are analyzed using the wavelet multiresolution technique, as described in Sec. II C. Here the signals are decomposed into 17 wavelet levels in which higher levels correspond to larger scale structures (lower frequency bands) while lower levels correspond to smaller scale structures (higher frequency bands). The central frequencies of different wavelet components of the acoustic and hydrodynamic pressure fluctuations are summarized in Table III. Such central frequencies represent various scales of turbulent structures. According to the central frequencies listed in Table III, the

TABLE III. Central frequencies of the wavelet components of acoustic and hydrodynamic pressure fluctuations. Note that the frequencies are normalized by the diameter of the cylinder and the free-stream velocity.

	A (6.6D, 170°)		D (4.6D, 170°)			A (6.6D, 170°)		D (4.6D, 170°)	
Level	f_A	f_H	f_A	f_H	Level	f_A	f_H	f_A	f_H
1	99.730	99.730	101.231	101.231	10	0.304	0.232	0.369	0.215
2	54.946	54.946	53.652	53.652	11	0.144	0.142	0.120	0.112
3	26.254	26.254	26.664	26.664	12	0.055	0.063	0.073	0.692
4	14.098	12.999	14.305	14.400	13	0.030	0.033	0.033	0.033
5	6.255	6.511	6.517	6.445	14	0.016	0.016	0.017	0.017
6	3.423	3.186	3.425	3.403	15	0.009	0.008	0.011	0.011
7	1.713	1.817	1.729	1.730	16	0.005	0.004	0.004	0.004
8	0.915	0.845	0.791	0.906	17	0.002	0.002	0.002	0.002
9	0.395	0.396	0.395	0.487					

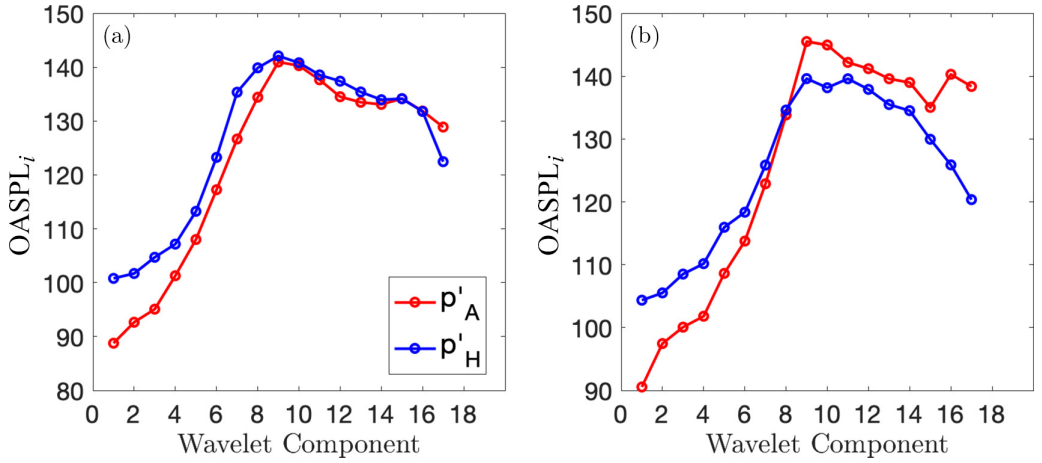

FIG. 24. The OASPL of different wavelet components of the acoustic and hydrodynamic pressure fluctuations at positions (a) A (6.6D, 170°) and (b) D (4.6D, 170°).

frequency band of the ninth wavelet component contains the fluctuating frequency of the separated shear layers (St = 0.4).

The sound and pseudo-sound signatures associated with different scale structures are assessed by computing the overall sound pressure level (OASPL) of each wavelet component of the acoustic and hydrodynamic pressure fluctuations. The OASPL is used as an indicator of the sound strength and has been defined in many references [36,37]. Similarly, the OASPL of the ith wavelet component (OASPL$_i$) of an acoustic or hydrodynamic pressure fluctuation is defined as

$$\mathrm{OASPL}_i = 20\log_{10}\left(\frac{p'_{i,\mathrm{rms}}}{p_{\mathrm{ref}}}\right), \tag{10}$$

where $p'_{i,\mathrm{rms}}$ is the root mean square of the ith wavelet component of acoustic or hydrodynamic pressure fluctuations and $p_{\mathrm{ref}} = 2 \times 10^{-5}$ Pa is the reference pressure. Figure 24 shows the OASPL of different wavelet components of the acoustic and hydrodynamic pressure fluctuations at positions A and D. At both positions, it is found that the ninth wavelet component of both acoustic and hydrodynamic pressure fluctuations, whose frequency bands contain the fluctuating frequency of the separated shear layers, contributes the most to the OASPL. This suggests that the vortical structure induced by the fluctuation of the separated shear layers is most closely related with the sound and pseudo-sound signatures. At position A, the hydrodynamic wavelet components have higher OASPL than the acoustic ones, with the disparity being larger for components at lower wavelet levels (higher frequency bands), as also suggested by the PSD in Fig. 18(a).

At position D, larger scale structures contribute more significantly to the acoustic OASPL than to the hydrodynamic OASPL, while smaller scale structures contribute more to the hydrodynamic OASPL than to the acoustic OASPL. For the acoustic wavelet components, an increase of OASPL at the 16th wavelet component reveals an important contribution to the sound generation from large-scale structures, which are probably related to the low-frequency expansion and compression waves. It should be noted that, for the hydrodynamic wavelet components, the ninth wavelet component and the 11th wavelet component contribute equivalently to the OASPL. However, at the central frequencies of the ninth and 11th wavelet component of the hydrodynamic pressure fluctuation, the PSD values differ. This is because the frequency band of the 11th wavelet component is narrower than that of the ninth; namely, a higher wavelet level corresponds to a narrower bandwidth.

IV. CONCLUSIONS

The vortex shedding behind a circular cylinder ceases at $\mathrm{Ma} = 0.9$. This paper explores the relative significance of radiating acoustic pressure fluctuations versus nonradiating hydrodynamic pressure fluctuations and their relationship with flow structures in the absence of detectable vortex shedding, elucidating an alternative noise generation mechanism of a circular cylinder in a quasi-steady transonic condition. First, a DNS of transonic flow past a circular cylinder is performed at $\mathrm{Re} = 3900$ and $\mathrm{Ma} = 0.9$. The flow contains complex features, i.e., formation of weak oblique shocks, expansion fans, compression waves, fluctuating separated shear layers, suppressed vortex shedding, λ shocks, and quasi-steady bow shocks. In the far field downstream of the λ shocks, a dominant tone at the fluctuating frequency of the separated shear layers is observed. Near-wake pressure fluctuations are more strongly correlated with far-field pressure fluctuations, whereas wall pressure fluctuations are uncorrelated with far-field pressure fluctuations, suggesting that the sound sources are located in the near wake rather than on the cylinder surface. Second, to quantitatively assess the radiating acoustic sound and the nonradiating hydrodynamic pseudo-sound generated by various flow features, the wavelet decomposition technique is applied to decompose the near-field pressure fluctuations, generated by various flow features, into the radiating acoustic pressure fluctuations and nonradiating hydrodynamic pressure fluctuations. In the near-field region just behind the λ shocks, as the distance from the fluctuating separated shear layer increases, the acoustic pressure fluctuation takes the place of the hydrodynamic pressure fluctuation as the dominant component of pressure fluctuations. In the region of expansion fans, the pressure fluctuation is principally a low-frequency acoustic pressure fluctuation. In the region of fluctuating separated shear layers, although the pressure fluctuation consists of a comparable amount of radiating acoustic and nonradiating hydrodynamic components at most frequencies, the pressure fluctuation mainly consists of radiating acoustic component at the fluctuating frequency of the separated shear layers. Overall, although expansion waves, compression waves, and their interactions with the λ shocks and the wake produce acoustic waves in the near field, the dominant acoustic waves are generated primarily by the fluctuation of the separated shear layers. Finally, a wavelet multiresolution analysis of the acoustic and hydrodynamic pressure fluctuations is conducted at two wake positions, one in the region just behind the λ shocks and the other in the region of the fluctuating separated shear layers. It is found that, among the various-scale structures, the vortical structure induced by the fluctuation of the separated shear layers is most closely related with both sound and pseudo-sound signatures. These findings provide valuable insight into noise control in aeronautical applications. This way focus of noise control can be given to the radiating acoustic component of pressure fluctuation and the most strongly radiating sound source region. The control of the oscillation of the separated shear layers, which is the main sound source in this problem, is expected to be an efficient way to achieve noise reduction.

ACKNOWLEDGMENTS

The author gratefully thanks Dr. Xiaohua Wu for insightful and helpful discussions and Dr. David Rival for his valuable comment on the initial draft. The computation/data handling were enabled by resources provided by the Digital Research Alliance of Canada and the National Academic Infrastructure for Supercomputing in Sweden (NAISS). The latter was partially funded by the Swedish Research Council through grant agreement No. 2022-06725.

APPENDIX

1. Calculation of the power spectral density

This Appendix shows how the power spectral density and the octave bin-averaged power spectral density are calculated. The discrete Fourier transform (DFT) of a windowed signal p, sampled at N_s

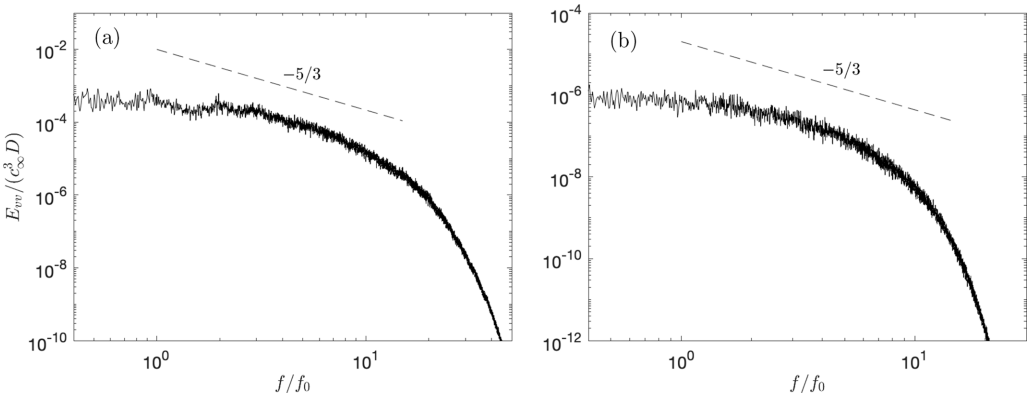

FIG. 25. Energy spectra of the vertical velocity fluctuation at two positions on the wake centerline: (a) $(5D, 180^\circ)$ and (b) $(32D, 180^\circ)$. The frequency is normalized by the tonal noise frequency at St = 0.4 (i.e., $f_0 = 0.4u_\infty/D$).

time steps with a time resolution of Δt, is given by Press *et al.* [69] as

$$C(f_k) = \sum_{j=1}^{N_s-1} p_j^{\text{win}} e^{-2\pi i jk/N_s} \qquad k = 0, \ldots, N_s - 1, \tag{A1}$$

where p_j^{win} is the time signal windowed by a Hann window and $f_k = k/(N_s\Delta t)$ represents the discretize frequency. The PSD is defined at $N_s/2 + 1$ frequencies as

$$\begin{aligned}
\Phi_{pp}(f_0) &= \frac{\Delta t}{N_s}[C(f_0)C^*(f_0)], \\
\Phi_{pp}(f_k) &= \frac{\Delta t}{N_s}\left[C(f_k)C^*(f_k) + C\left(f_{N_s-k}\right)C^*\left(f_{N_s-k}\right)\right] \quad k = 1, \ldots, N_s/2 - 1, \\
\Phi_{pp}\left(f_{N_s/2}\right) &= \frac{\Delta t}{N_s}\left[C\left(f_{N_s/2}\right)C^*\left(f_{N_s/2}\right)\right],
\end{aligned} \tag{A2}$$

where $C^*(f_k)$ is the complex conjugate of $C(f_k)$.

Assume that the PSD of a time signal, $\Phi_{pp}(f)$, is a piecewise continuous function, the bin-averaged PSD is given in Khalighi [70] as

$$\Phi_{pp}(f_{\text{cen}}) = \frac{1}{f_{\max} - f_{\min}} \int_{f_{\min}}^{f_{\max}} \Phi_{pp}(f)\, df, \tag{A3}$$

where f_{cen}, $f_{\min}$, and $f_{\max}$ are the frequencies at the center, lower, and upper boundaries of a bin, respectively. In this paper, the octave bin averaging is used. Each octave band in the frequency is logarithmically spaced in n intervals and averaged, which is called the $1/n$ octave bin averaging. The PSD at each bin is presented in the center frequency, calculated as $f_{\text{cen}} = \sqrt{f_{\min} f_{\max}}$. In the present study, the $1/6$ octave bin averaging is applied to smooth the spectra.

2. Energy spectra of the vertical velocity fluctuation

Figure 25 shows the energy spectra of the vertical velocity fluctuation at a near-field position $(x = 5D)$ and a far-field position $(x = 32D)$ on the wake centerline. The predicted turbulence decay rate at both positions is close to the Kolmogorov $-5/3$ slope, indicating the sufficiency of the current grid resolution. It is also observed that the level of the spectrum at $x = 5D$ is more than two orders

of magnitude higher than that at $x = 32D$, indicating that, at a distance of $32D$ in the downstream wake, turbulence has significantly decayed.

[1] P. Beaudan and P. Moin, Numerical experiments on the flow past a circular cylinder at sub-critical Reynolds number, Tech. Rep. No. TF-62, Department of Mechanical Engineering, Stanford University, 1994.

[2] L. Ong and J. Wallace, The velocity field of the turbulent very near wake of a circular cylinder, Exp. Fluids **20**, 441 (1996).

[3] A. G. Kravchenko and P. Moin, Numerical studies of flow over a circular cylinder at $\mathrm{Re}_D = 3900$, Phys. Fluids **12**, 403 (2000).

[4] P. Parnaudeau, J. Carlier, D. Heitz, and E. Lamballais, Experimental and numerical studies of the flow over a circular cylinder at Reynolds number 3900, Phys. Fluids **20**, 085101 (2008).

[5] C. Williamson, The existence of two stages in the transition to three-dimensionality of a cylinder wake, Phys. Fluids **31**, 3165 (1988).

[6] H.-Q. Zhang, U. Fey, B. R. Noack, M. König, and H. Eckelmann, On the transition of the cylinder wake, Phys. Fluids **7**, 779 (1995).

[7] C. Williamson, Mode a secondary instability in wake transition, Phys. Fluids **8**, 1680 (1996).

[8] S. Behara and S. Mittal, Wake transition in flow past a circular cylinder, Phys. Fluids **22**, 114104 (2010).

[9] U. Fey, M. König, and H. Eckelmann, A new Strouhal–Reynolds-number relationship for the circular cylinder in the range $47 < \mathrm{Re} < 2 \times 10^5$, Phys. Fluids **10**, 1547 (1998).

[10] T. Nagata, A. Noguchi, K. Kusama, T. Nonomura, A. Komuro, A. Ando, and K. Asai, Experimental investigation on compressible flow over a circular cylinder at Reynolds number of between 1000 and 5000, J. Fluid Mech. **893**, A13 (2020).

[11] O. Inoue and N. Hatakeyama, Sound generation by a two-dimensional circular cylinder in a uniform flow, J. Fluid Mech. **471**, 285 (2002).

[12] Y. Khalighi, A. Mani, F. Ham, and P. Moin, Prediction of sound generated by complex flows at low Mach numbers, AIAA J. **48**, 306 (2010).

[13] Y. Oguma, T. Yamagata, and N. Fujisawa, Measurement of sound source distribution around a circular cylinder in a uniform flow by combined particle image velocimetry and microphone technique, J. Wind Eng. Ind. Aerodyn. **118**, 1 (2013).

[14] D. A. Lysenko, I. Ertesvåg, and K. Rian, Towards simulation of far-field aerodynamic sound from a circular cylinder using openfoam, Int. J. Aeroacoust. **13**, 141 (2014).

[15] E. Berger and R. Wille, Periodic flow phenomena, Annu. Rev. Fluid Mech. **4**, 313 (1972).

[16] C. Norberg, Effects of Reynolds number and a low-intensity freestream turbulence on the flow around a circular cylinder, Ph.D. thesis, Chalmers University of Technology, Goteborg, Sweden, Technological Publications 87(2) (1987), pp. 1–55.

[17] C. H. Williamson, Vortex dynamics in the cylinder wake, Annu. Rev. Fluid Mech. **28**, 477 (1996).

[18] M. Zdravkovich, Different modes of vortex shedding: An overview, J. Fluids Struct. **10**, 427 (1996).

[19] J. Gerrard, The mechanics of the formation region of vortices behind bluff bodies, J. Fluid Mech. **25**, 401 (1966).

[20] A. Mani, J. Larsson, and P. Moin, Suitability of artificial bulk viscosity for large-eddy simulation of turbulent flows with shocks, J. Comput. Phys. **228**, 7368 (2009).

[21] A. Mani, Optical distortions by compressible turbulence, Ph.D. thesis, Stanford University, 2009.

[22] M. Couliou and V. Brion, State switching in the wake of a transverse circular cylinder in the transonic regime, Phys. Fluids **35**, 116115 (2023).

[23] V. Murthy and W. Rose, Form drag, skin friction, and vortex shedding frequencies for subsonic and transonic crossflows on circular cylinder, in *10th Fluid and Plasmadynamics Conference, Albuquerque, NM* (AIAA, Reston, VA, 1977), AIAA Paper 77–687.

[24] V. Murthy and W. Rose, Detailed measurements on a circular cylinder in cross flow, AIAA J. **16**, 549 (1978).
[25] C. Xu, L. Chen, and X. Lu, Effect of Mach number on transonic flow past a circular cylinder, Sci. Bull. **54**, 1886 (2009).
[26] C.-Y. Xu, L.-W. Chen, and X.-Y. Lu, Numerical simulation of shock wave and turbulence interaction over a circular cylinder, Mod. Phys. Lett. B **23**, 233 (2009).
[27] Z. Xia, Z. Xiao, Y. Shi, and S. Chen, Mach number effect of compressible flow around a circular cylinder, AIAA J. **54**, 2004 (2016).
[28] A. Tamura and M. Tsutahara, Direct simulation of aeolian tones emitted from a circular cylinder in transonic flows using the finite difference lattice boltzmann method, Fluid Dyn. Res. **42**, 015007 (2010).
[29] B. Etkin, G. K. Korbacher, and R. T. Keefe, Acoustic radiation from a stationary cylinder in a fluid stream (aeolian tones), J. Acoust. Soc. Am. **29**, 30 (1957).
[30] J. H. Gerrard, Measurements of the sound from circular cylinders in an air stream, Proc. Phys. Soc. London B **68**, 453 (1955).
[31] S. Li, D. E. Rival, and X. Wu, Sound source and pseudo-sound in the near field of a circular cylinder in subsonic conditions, J. Fluid Mech. **919**, A43 (2021).
[32] R. Maryami, E. J. Arcondoulis, and Y. Liu, Flow and aerodynamic noise control of a circular cylinder by local blowing, J. Fluid Mech. **980**, A56 (2024).
[33] O. Rodriguez, The circular cylinder in subsonic and transonic flow, AIAA J. **22**, 1713 (1984).
[34] C. E. Tinney, P. Jordan, A. M. Hall, J. Delville, and M. N. Glauser, A time-resolved estimate of the turbulence and sound source mechanisms in a subsonic jet flow, J. Turbul. **8**, N7 (2007).
[35] C. E. Tinney and P. Jordan, The near pressure field of co-axial subsonic jets, J. Fluid Mech. **611**, 175 (2008).
[36] S. Grizzi and R. Camussi, Wavelet analysis of near-field pressure fluctuations generated by a subsonic jet, J. Fluid Mech. **698**, 93 (2012).
[37] M. Mancinelli, T. Pagliaroli, A. Di Marco, R. Camussi, and T. Castelain, Wavelet decomposition of hydrodynamic and acoustic pressures in the near field of the jet, J. Fluid Mech. **813**, 716 (2017).
[38] S. K. Lele, Compact finite difference schemes with spectral-like resolution, J. Comput. Phys. **103**, 16 (1992).
[39] R. M. Beam and R. F. Warming, An implicit finite-difference algorithm for hyperbolic systems in conservation-law form, J. Comput. Phys. **22**, 87 (1976).
[40] M. Giles, Nonreflecting boundary conditions for euler equation calculations, AIAA J. **28**, 2050 (1990).
[41] S. S. Collis, A computational investigation of receptivity in high-speed flow near a swept leading-edge, Ph.D. thesis, Stanford University, 1997.
[42] S. Nagarajan, S. K. Lele, and J. H. Ferziger, A robust high-order compact method for large eddy simulation, J. Comput. Phys. **191**, 392 (2003).
[43] A. Mani, M. Wang, and P. Moin, Resolution requirements for aero-optical simulations, J. Comput. Phys. **227**, 9008 (2008).
[44] A. Mani, P. Moin, and M. Wang, Computational study of optical distortions by separated shear layers and turbulent wakes, J. Fluid Mech. **625**, 273 (2009).
[45] O. Lehmkuhl, I. Rodríguez, R. Borrell, and A. Oliva, Low-frequency unsteadiness in the vortex formation region of a circular cylinder, Phys. Fluids **25**, 085109 (2013).
[46] J. W. Wu, Direct numerical simulation of flow over circular cylinders for large-eddy simulation modeling, Ph.D. thesis, University of Illinois at Urbana-Champaign, 2001.
[47] W. J. Pinto, F. Margnat, and C. Nous, Influence of the length of a cylinder on its Aeolian Tone Level: Measurement and modelling, in *14th WCCM-ECCOMAS Congress* (CIMNE, Paris, France, 2021), Vol. 1500.
[48] K. Karthik, S. Vengadesan, and S. Bhattacharyya, Prediction of flow induced sound generated by cross flow past finite length circular cylinders, J. Acoust. Soc. Am. **143**, 260 (2018).
[49] C. Meneveau, Analysis of turbulence in the orthonormal wavelet representation, J. Fluid Mech. **232**, 469 (1991).

[50] T. Suzuki and T. Colonius, Instability waves in a subsonic round jet detected using a near-field phased microphone array, J. Fluid Mech. **565**, 197 (2006).
[51] H. S. Ribner, Aerodynamic sound from fluid dilitations: A theory of the sound from jets and other flows (Institute of Aerophysics, University of Toronto, 1962).
[52] J. F. Williams, Hydrodynamic noise, Annu. Rev. Fluid Mech. **1**, 197 (1969).
[53] J. Ristorcelli, A pseudo-sound constitutive relationship for the dilatational covariances in compressible turbulence, J. Fluid Mech. **347**, 37 (1997).
[54] D. L. Donoho and J. M. Johnstone, Ideal spatial adaptation by wavelet shrinkage, Biometrika **81**, 425 (1994).
[55] B. Vidakovic, *Statistical Modeling by Wavelets* (John Wiley & Sons, 2009).
[56] D. B. Percival and A. T. Walden, *Wavelet Methods for Time Series Analysis*, Cambridge Series in Statistical and Probabilistic Mathematics (Cambridge University Press, 2000).
[57] D. B. Percival and H. O. Mofjeld, Analysis of subtidal coastal sea level fluctuations using wavelets, J. Am. Stat. Assoc. **92**, 868 (1997).
[58] B. Whitcher, P. Guttorp, and D. B. Percival, Wavelet analysis of covariance with application to atmospheric time series, J. Geophys. Res.: Atmos. **105**, 14941 (2000).
[59] X. Wu, B. Yu, and Y. Wang, Wavelet analysis on turbulent structure in drag-reducing channel flow based on direct numerical simulation, Adv. Mech. Eng. **5**, 514325 (2013).
[60] O. M. Phillips, On the generation of sound by supersonic turbulent shear layers, J. Fluid Mech. **9**, 1 (1960).
[61] T. Colonius, S. K. Lele, and P. Moin, Sound generation in a mixing layer, J. Fluid Mech. **330**, 375 (1997).
[62] R. Ida, Y. Tamaki, and S. Kawai, Theoretical link in numerical shock thickness and shock-capturing dissipation, J. Comput. Phys. **505**, 112901 (2024).
[63] A. Puckett and H. Stewart, The thickness of a shock wave in air, Q. Appl. Math. **7**, 457 (1950).
[64] P. K. Kundu, I. M. Cohen, and D. R. Dowling, *Fluid Mechanics* (Elsevier, Amsterdam, 2012), p. 891.
[65] L. Guo, X. Zhang, and G. He, Large-eddy simulation of circular cylinder flow at subcritical Reynolds number: Turbulent wake and sound radiation, Acta Mechanica Sinica **32**, 1 (2016).
[66] X. Liu, D. J. Thompson, and Z. Hu, Numerical investigation of aerodynamic noise generated by circular cylinders in cross-flow at Reynolds numbers in the upper subcritical and critical regimes, Int. J. Aeroacoust. **18**, 470 (2019).
[67] N. Curle, The influence of solid boundaries upon aerodynamic sound, Proc. R. Soc. London A **231**, 505 (1955).
[68] D. W. Scott, *Multivariate Density Estimation: Theory, Practice, and Visualization* (John Wiley & Sons, 1992).
[69] W. H. Press, S. A. Teukolsky, B. P. Flannery, and W. T. Vetterling, *Numerical recipes in Fortran 77: The art of scientific computing*, volume 1 of Fortran numerical recipes (Cambridge University Press, 1992).
[70] Y. Khalighi, Computational aeroacoustics of complex flows at low Mach number, Ph.D. thesis, Stanford University, 2010.